Soil Dynamics and Earthquake Engineering 187 (2024) 109009

Contents lists available at ScienceDirect

Soil Dynamics and Earthquake Engineering

journal homepage: www.elsevier.com/locate/soildyn

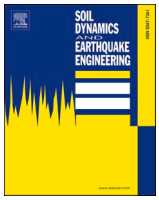

AI-driven predictions of the dynamic properties of fine-grained soils in South Italy based on laboratory testing

Michele Placido Antonio Gatto [a,*], Francesco Castelli [b], Valentina Lentini [b], Lorella Montrasio [a]

[a] Department of Civil, Environmental, Architectural Engineering, and Mathematics, University of Brescia, Via Branze 38, 25123, Brescia, Italy
[b] Faculty of Engineering and Architecture, University Kore of Enna, Via delle Olimpiadi, 94100, Enna, Italy

ARTICLE INFO

Keywords:
Dynamic properties
Laboratory tests
Fine-grained soils
Artificial intelligence
Geotechnical earthquake engineering

ABSTRACT

This study presents the use of Artificial Intelligence (AI) to predict the dynamic behaviour of fine-grained soils of South Italy based on a detailed laboratory investigation. The investigation consists of Resonant Column (RC), Cyclic Torsional Shear (CTS), and Cyclic Triaxial (CTx) tests performed on 25 specimens of fine-grained soils retrieved from 11 sites in Sicily (South Italy). To develop accurate predictive models of soil dynamic properties, essential for site response analyses and dynamic soil-structure interaction, various regression techniques were applied. These techniques range from Multiple Linear Regression (MLR) to more complex AI methods, specifically Machine Learning (ML) and Deep Learning (DL) based on FeedForward Neural networks (FFN). Three predictive models were developed to derive strain-dependent shear modulus (G), damping ratio (D), and normalized shear modulus (G/G_0), using four inputs: shear strain (γ), plasticity index (PI), confining pressure (p'_0), and the Over Consolidation Ratio (OCR). To determine the optimal FFN topology, 1350 networks were developed by varying hidden layers (1–3), hidden neurons (1–50 per layer), and activation functions (ReLU, sigmoid and hyperbolic tangent). Hybrid FFN optimised through Genetic Algorithm and Particle Swarm Optimization techniques were also investigated. Single-hidden layer networks with fewer than 15 neurons provided acceptable predictions (R^2_{test} of 0.97 for G-γ, 0.93 for G/G_0-γ, and 0.85 for D-γ models). Multiple-hidden layer networks yielded higher accuracy for G and D models but are more complex for practical use. The FFN models outperformed MLR and other established empirical formulations, highlighting the site-specificity of the modelling parameters of the latter.

1. Introduction

Dynamic properties of soils, i.e., the shear modulus G and the damping ratio D, play a key role in the response of structures subjected to time-varying loads, deriving from earthquakes or vibrations (e.g., traffic-induced): it deals with strain-dependent characteristics that change with the level of induced strain γ. According to seismic standards, such as Eurocode 8 [1] or NTC-18 [2], the design of structures to support seismic loads is done through the linear static analysis, consisting in the application of horizontal forces, whose amplitude depends on the site amplification (given by the local stratigraphy and topology) [3–5]. To this aim, site response analysis, commonly requiring the knowledge of the dynamic properties, is therefore relevant [6–10]. Also, the stress-strain response of structures subjected to dynamic loads is affected by the foundation soil and its dynamic properties. To this end, studies of soil-structure interaction are commonly conducted, e.g., through finite element numerical modelling where the strain-dependent properties of the soil are fundamental [11–15]. Recently, several examples of performed-based design (probabilistic approach) accounting for the dynamic properties of soils have been shown by literature [16–18].

The determination of the dynamic properties of soils presents a myriad of challenges, due to a complex stress-strain behaviour. Depending on the strain range to be captured, specific tests are traditionally conducted. Small-strain dynamic properties can be derived from laboratory tests, such as Resonant Column Test (RC), Cyclic Torsional Test (CTS) and Cyclic Triaxial Test (CTx), or from field tests, such as MASW (Multichannel Analysis of Surface Waves) and SASW (Spectral Analysis of Surface Waves). The latter allow us to derive the small-strain shear modulus from the measurement of the shear wave velocity V_s or

* Corresponding author.
E-mail addresses: michele.gatto@unibs.it (M.P.A. Gatto), francesco.castelli@unikore.it (F. Castelli), valentina.lentini@unikore.it (V. Lentini), lorella.montrasio@unibs.it (L. Montrasio).

https://doi.org/10.1016/j.soildyn.2024.109009
Received 3 August 2024; Received in revised form 18 September 2024; Accepted 2 October 2024

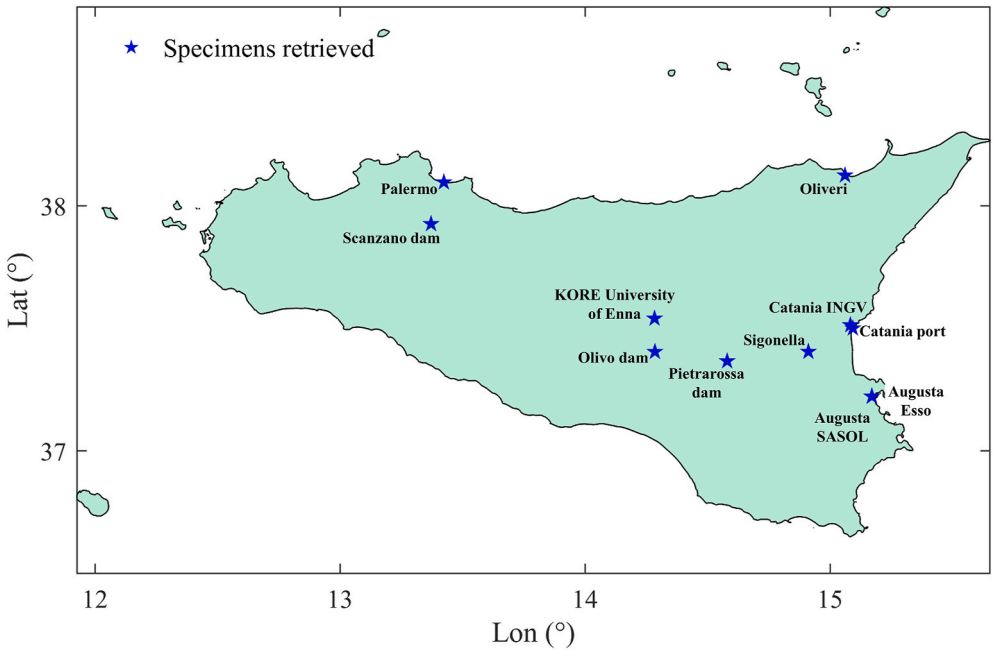

Fig. 1. Location of 11 boreholes where the 25 specimens were retrieved.

the damping ratio from the analysis of the spatial attenuation of Rayleigh surface waves [19,20]. Medium-to large-strain properties are mainly derived from laboratory tests [21,22]; several attempts have been done to derive them even from field tests, but only few large strain levels have been investigated [23]. Clearly, results of fields tests are more likely to be representative of true soil behaviour, while the dynamic soil properties derived at laboratory could misrepresent the reality due to sampling disturbance and laboratory difficulties in replicating field conditions (anisotropic stress states or scale effects, the latter affecting the behaviour of heterogeneous soils).

Many research studies have showed the results of the above mentioned experimental tests performed on different soils. The main evidence is that there are several key parameters depending on the soil type that affect both the amplitude and the shape of G-γ and D-γ curves: the relative density or the coefficient of uniformity for coarse-grained soils [24–26], the plasticity index PI and the over consolidation ratio OCR for fine-grained soils [21,27–31]. Then, the dynamic behaviour of all the soil type changes also with the confining pressure p'_0, the loading frequency and the number of loading cycles [32,33]. More recently, the effects of temperature, aging or the water content have been investigated [34–36].

Stress-strain behaviour of soils under dynamic loads is complex and its analysis through field and laboratory measurements is often expensive and time-consuming [37]. Researchers derive empirical formulations to extend available experimental results to other applications. Hardin and Drnevich [38] modelled the G decay through hyperbolic relationship, with specific modelling parameters whose values change depending on the soil type, later improved by other studies [29,32,39–41]. D-curves has been typically modelled as a function of G/G_0 and other soil-dependent parameters. Further, there are formulations, different from the hyperbolic one, coming from extensive regression techniques applied on the results of laboratory tests [42]. In all cases, modelling parameters need to be calibrated on experimental results because they are site-specific [43–46].

Despite of the calibration of the modelling parameters, empirical models could not provide good fit of the experimental results. As an example, Dammala et al. [44] found better accuracy by adopting Darendeli's formulation [40] (coefficient of correlation R^2 around 96 % for the normalized shear modulus, 82 % for the damping ratio), rather than the ones provided by Ishibashi and Zhang [32] or Seed and Idriss [39], which underestimate the modulus degradation. For this reason, such models should be carefully applied on studies of site effects or soil-structure interaction to obtain reliable results. Yılmaz and Zehtab [47] demonstrated that amplification derived by performing an equivalent-linear site response analysis with strain-modulus-damping relationships proposed by literature underestimates the site amplification factors. This means that accuracy of modelling of the soil dynamic properties is still a challenging issue mainly because of the complexity of the soil behaviour [36].

Among the data-driven methods to derive predictive models, Artificial intelligence (AI) is demonstrating potential in enhancing the ability to interpret and extrapolate from existing data. AI techniques, including Machine Learning (ML) and Deep Learning (DL), offer the potential to identify patterns and relationships in large, multidimensional datasets that may not be apparent through traditional analytical approaches. AI has emerged as a powerful tool in various fields of engineering, and geotechnical earthquake engineering is no exception [48,49]. In recent years, it has been increasingly applied to address complex geotechnical problems; notable examples include the use of artificial neural networks (ANNs) for predicting soil properties, support vector machines (SVMs) for soil classification, and genetic algorithms (GAs) for optimization of geotechnical designs [36,50–59]. The application of AI in geotechnical engineering leverages the abundance of data generated from laboratory tests, field measurements, and numerical simulations. However, it is crucial to note that the effectiveness of AI methods is intrinsically linked to the quality and representativeness of the underlying data.

This study presents the dynamic characterisation of fine-grained soils from Sicily (South Italy) based on RC, CTS and CTx tests. Regression analysis using ML and DL algorithms is then applied to 70 % of the experimental dataset to derive models for predicting the values of G, G/G_0 and D, based on strain level, PI, OCR and p'_0 - all inputs derived from traditional geotechnical characterisation preceding the definition of the geotechnical model. The aim is to demonstrate how the use of artificial intelligence can yield models for predicting dynamic properties that may perform better than existing empirical models. Furthermore, it examines whether model complexity is synonymous with accuracy, with a focus on developing models that are both accurate and easily useable by practitioners. Additionally, it highlights the need for a very extensive

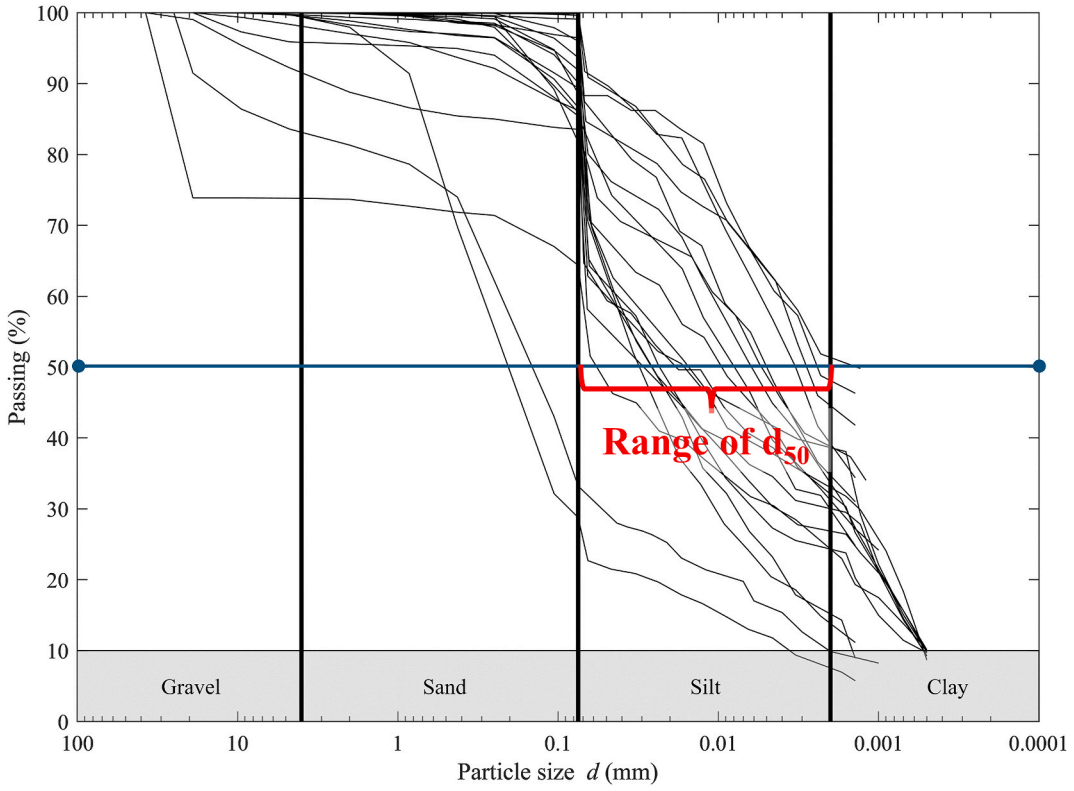

Fig. 2. Particle size distribution of the specimens.

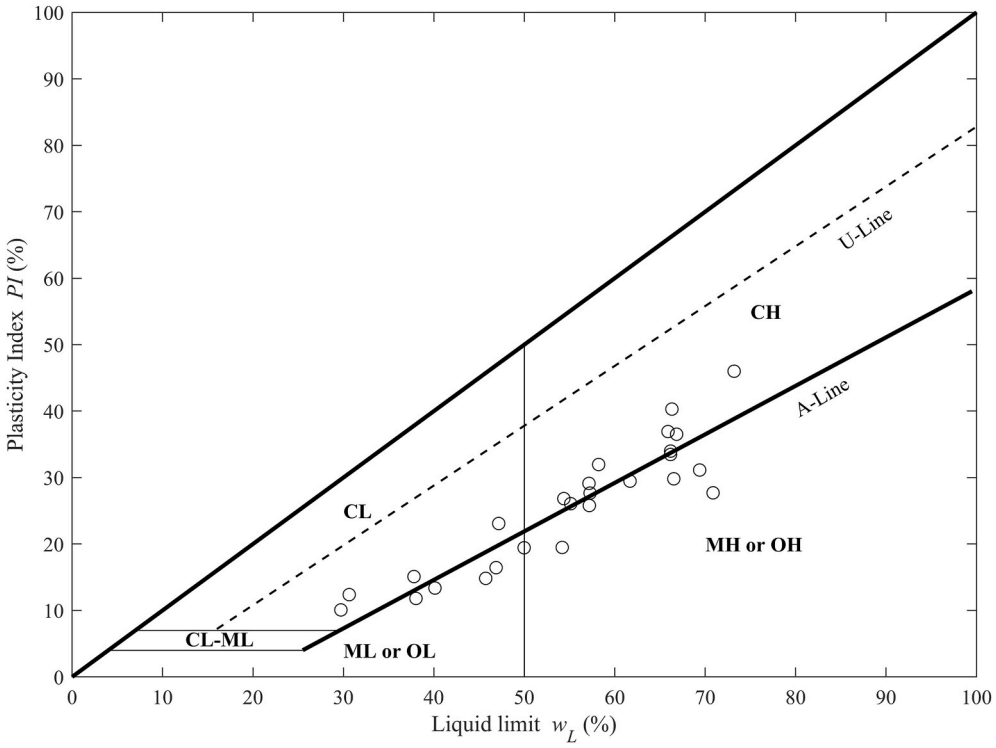

Fig. 3. Casagrande chart. The A-line separates clays (C) from silts (M), while the value of the liquid limit w_L of 50 % separates fine-grained soils with low plasticity (L) from those with high plasticity (H).

database to develop models with broader applicability. Section 2 describes the database preparation, including the classification and dynamic characterisation of the fine-grained soils involved. Section 3 explains the regression techniques adopted and their application to the developed dataset. Section 4 details the development of ANN models, including the identification of the best topologies and activation

Table 1
Summary of borehole locations, number of specimens retrieved per borehole, sampling depth, plasticity index, and tests performed.

Location	No. Of specimens retrieved	Specimen label	Depth (m)	*PI* (%)	USCS classification	Tests performed
Augusta - Esso	3	S1C1	4.5–5	33.98	CH	RC, CTS
		S1C2	13–13.5	29.12	CH	RC, CTS, CTx
		S2C1	11.4–11.9	36.52	CH	RC,CTS
Augusta - SASOL	2	S1C1	2.00–2.50	29.46	MH	RC,CTS
		S1C3	18–18.5	31.13	MH	RC,CTS
Olivo dam	1	SV313	28.00–28.40	40.30	CH	RC
Pietrarossa dam	4	SV0CI7	24.00–24.50	31.96	CH	CTx
		SV1CI4	18.50–19.00	16.44	ML	CTx
		SV1CI7	36.00–36.50	23.08	CL	CTx
		SV2CI6	22.50–23.00	26.83	CH	CTx
Scanzano dam	2	S1C2	8–8.5	19.48	MH	CTx
		S2C2	7.3–7.8	14.83	ML	RC
Eurospin	1	S1C2	15.00–15.50	27.66	CH	RC,CTS
KORE new buildings	1	S1C2	6.00–6.20	33.47	MH	RC
Oliveri (ME)	2	SA1C1	20–20.5	10.08	CL	RC
		SA11C3	10–10.5	11.20	CL	RC
Sigonella	3	S1CI3	17.50–18.00	13.37	ML	RC,CTS
		S1CI4	25.50–26.00	11.81	ML	RC,CTS
		S3bCI1	2.70–3.20	19.43	ML	RC,CTS
INGV Catania	4	S1C1	4.00–4.50	–	–	RC
		S2C3	14.00–14.50	–	–	RC
		S2C5	72.00–72.50	–	–	RC
		S3C1	5.50–5.90	–	–	RC
Catania port	2	S06-SPT - FC2	35–35.5	15.1	CL	RC
		S06-SPT - FC4	46.4–46.9	15.1	CL	RC

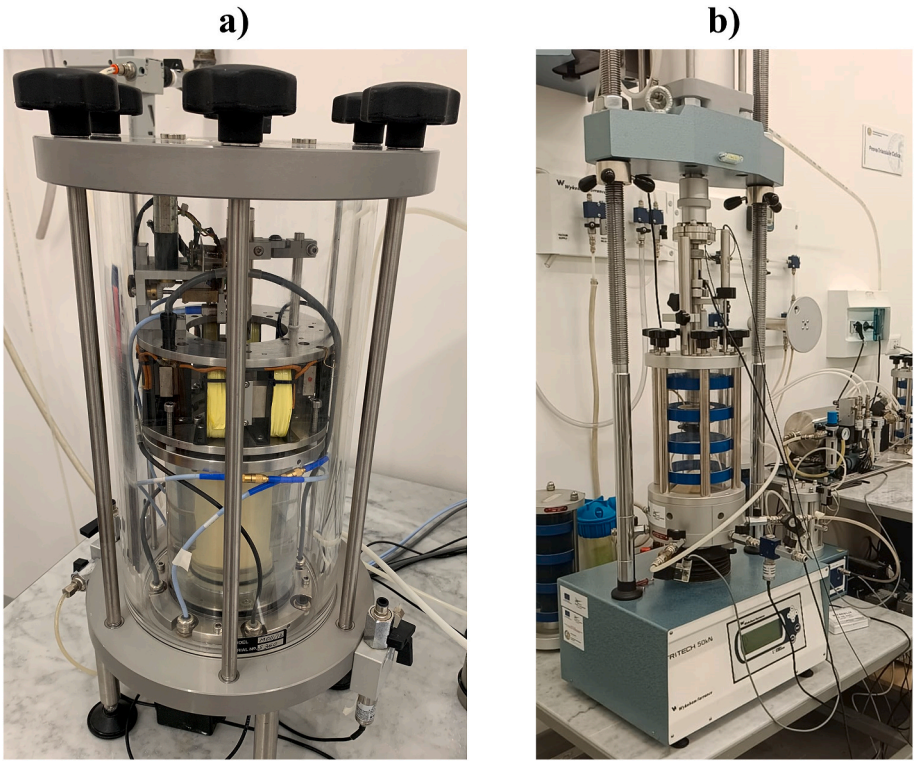

Fig. 4. Devices available at the Soil Dynamics and Geotechnical Engineering Laboratory of the University KORE of Enna (Italy) for a) dynamic (combined RC-CTS); and b) cyclic tests (CTx).

functions. The performance of ANN models is then compared with that of simple regression techniques as well as the one of existing and well-established empirical formulation. Finally, Section 5 discusses the results, highlighting the need for model calibration and the potential of ML techniques to provide accurate predictions of soil dynamic properties.

2. Database of the laboratory testing

Laboratory tests were carried out for seismic microzonation purposes. The database includes the experimental results obtained from 25 specimens retrieved from 11 sites in Sicily. The positions of the boreholes are shown in Fig. 1. Undisturbed specimens were received at the Soil Dynamics and Geotechnical Engineering Laboratory of the University KORE of Enna in cylindrical sampling tubes (diameter 8 cm, 50

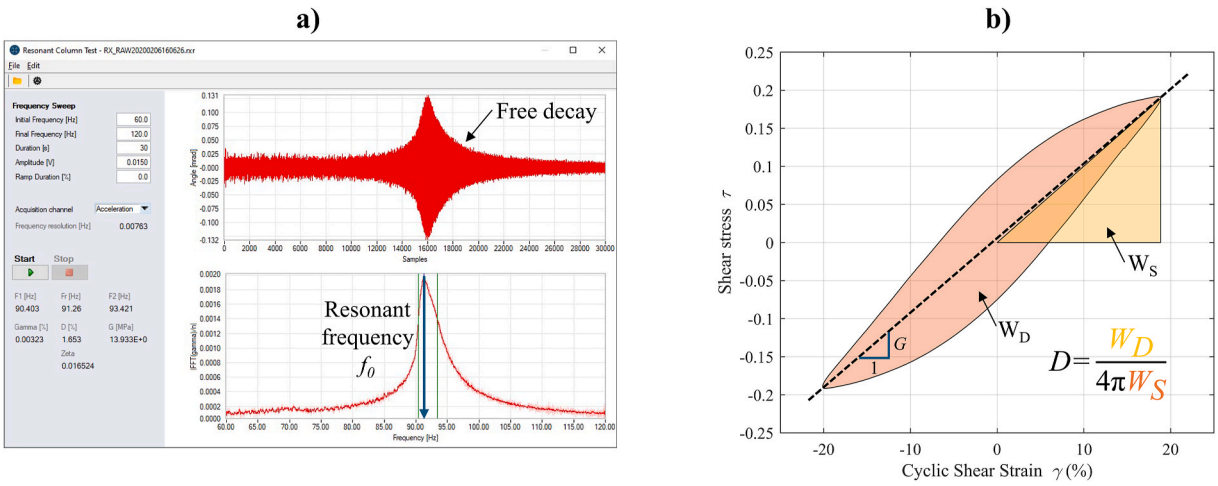

Fig. 5. Typical results from RC-CTS and CTx tests. a) Illustration of resonant frequency detection and the free decay at the resonant frequency in RC tests; b) hysteresis loop and derivation of the shear modulus (G) and damping ratio (D). Note that in CTx, similar loops are measured with the axial strain (ε_a) on the x-axis and the deviatoric stress (q) on the y-axis.

cm long), maintaining their original moisture content. Upon receipt, the samples were verified to be intact and properly sealed. To preserve their in-situ characteristics, the specimens were stored under controlled environmental conditions at a constant temperature of 22 °C prior to testing.

As a first step, samples were opened and qualitatively recognised (ASTM D2487; ASTM D2488). The soil type was then properly identified through standard soil classification tests, such as sieve analysis (ASTM D421; ASTM D422; ASTM D2217) and Atterberg's limits (ASTM D4318). RC, CTS and CTx tests were performed to determine the dynamic properties of each specimen, following specific standards (ASTM D4015; ASTM D3999; ASTM D5311).

2.1. Soil classification

The ASTM D2487 standard (Unified Soil Classification System, USCS) was followed to determine the soil type through "classification", based on the results of sieve analysis and Atterberg's limits. Sieve analysis was conducted using a set of standard sieves to derive the particle size distribution, plotted as the percentage of mass passing each sieve versus particle size. Atterberg's limits involved evaluating the liquid and plastic limits (w_L and w_P, respectively). The Plasticity Index PI was derived as w_L - w_P. Atterberg's limits and PI were used to classify the mass passing the No. 200 sieve (when greater than 12 %) using the Casagrande chart, where pairs of w_L and PI were plotted.

The particle size distribution of the analysed specimens is shown in Fig. 2. The average particle size, represented by d_{50}, (i.e., the diameter of the soil passing at 50 %), is smaller than 0.075 mm, typical of fine-grained soils (silts and clays). The Casagrande chart in Fig. 3 shows that almost all points lie on the A-line, separating clays (C) from silts (M), suggesting no particular type of fine-grained soils among the specimens.

Table 1 summarises the borehole locations, the number of specimens retrieved, the depth, PI and the tests performed, which are described in the next Section.

2.2. RC, CTS and TXC: a brief overview of the dynamic and cyclic tests

Stress-controlled RC and CTS tests, and strain-controlled CTx tests were performed through the devices shown in Fig. 4. RC and CTS tests were conducted using a combined apparatus, while CTx tests were performed through a Triaxial cell equipped to apply cyclic loads. RC and CTS tests are useful for analysing small to medium strain properties, while CTx tests provide valuable insights into large strain behaviour. The combination of data from the three tests allows for a comprehensive dynamic characterisation of the fine-grained soils across various strain levels and loading conditions.

The combined RC-CTS apparatus includes a torsional motor (electromagnetic driving system) which applies a cyclic torque following a sinusoidal function. The amplitude of the sine wave is expressed in volts and controlled through a specific sine wave generator. The frequency of the sine function is constant in CTS, while in RC tests it is varied until the resonant frequency of the specimen is reached. Since the dynamic behaviour of soil is frequency-dependent, the selection of the frequency in CTS tests is crucial: to maintain consistency with typical earthquake loading rates, the frequency of 0.5 Hz is chosen. In CTx tests, the cyclic load is applied axially through a contrast equipped with an electro-pneumatic system. Before applying the cyclic load, all tests follow an initial phase consisting of: i) back-pressure application, preventing the swelling of the specimen; ii) saturation of the specimen, ending when the B-Skempton parameter is at least to 0.95; iii) application of the confining pressure through the cell water. Each specimen is subjected to a confining pressure equal to the effective isotropic stress at the sampling depth. During the application of the cyclic load, all the tests are performed with closed drainage, so that the undrained conditions are reproduced, similar to what happens during earthquakes.

The evaluation of G and D varying with the strain level γ is based on the response of the specimen, which is measured through sensors installed at the top cap. In RC tests, position sensors detect the rotation of the head of the electromagnetic motor; the measured rotation is plotted against the frequency of the applied torque, which is changed linearly until resonance is observed. The resonant frequency f_0 is taken as the one establishing the maximum rotation. From f_0, solving the equations of one-dimensional wave propagation problem with regard to angular deformation, the shear wave velocity V_s can be evaluated, and therefore the shear modulus:

$$V_s = 2\pi L \frac{f_0}{F_T} \tag{1a}$$

$$G = \rho V_s^2 \tag{1b}$$

where L is the specimen length, F_T a dimensionless frequency factor (function of the ratio between the polar mass moment of inertia of the top platen and the one of the soil specimen) and ρ the soil density. This solution assumes the soil behaviour as linear elastic, true for small strains. The specimen is then excited with a signal having a frequency equal to or near the resonant frequency. After a certain period, the

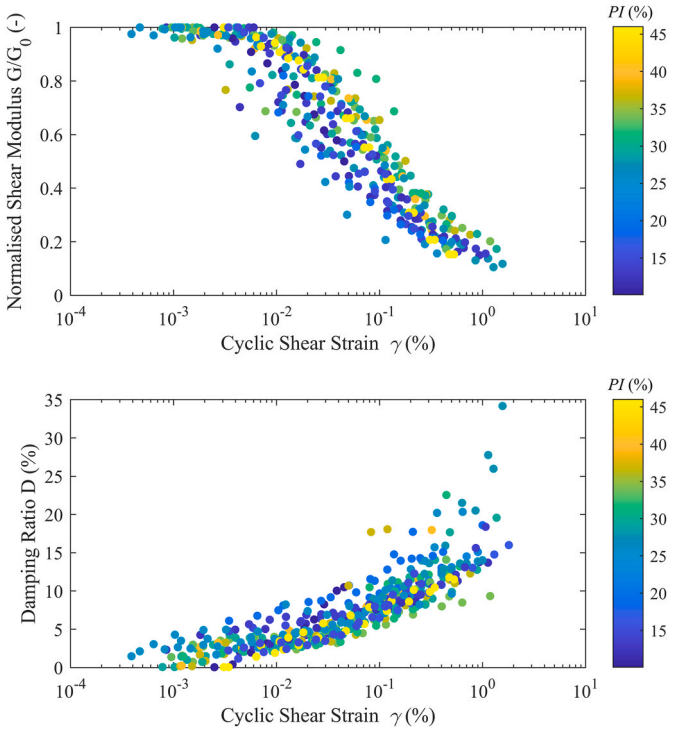

Fig. 6. Strain-dependent normalized shear modulus (G/G_0) and damping ratio (D) varying with the plasticity index PI.

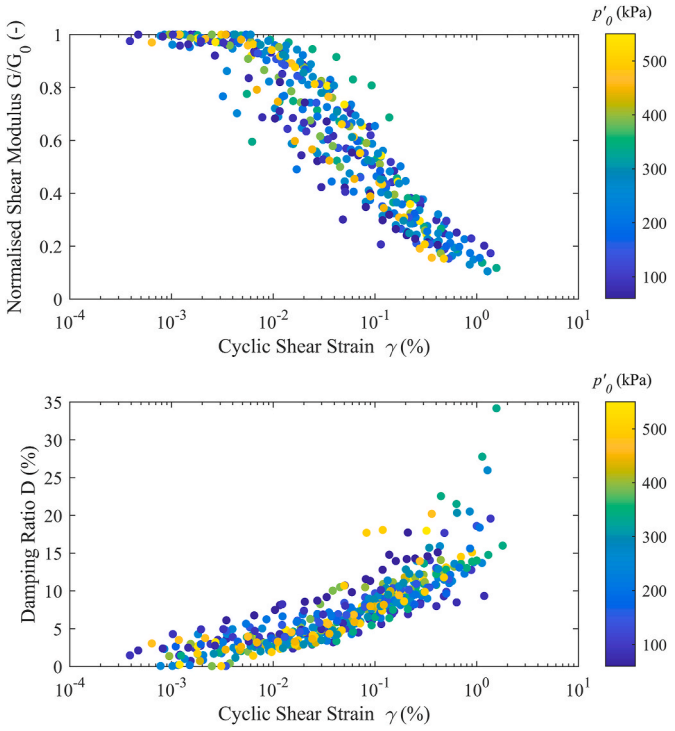

Fig. 7. Strain-dependent normalized shear modulus (G/G_0) and damping ratio (D) varying with the confining pressure (p'_0).

specimen is left free to oscillate, and the free decay method is applied to evaluate damping. Fig. 5a shows how the resonant frequency is detected and an example of free decay. In both CTS and CTx, stress excitation is plotted against the strain response, usually deriving ellipses. For CTS, shear stress-shear strain (τ-γ) is plotted, while for CTx the deviatoric

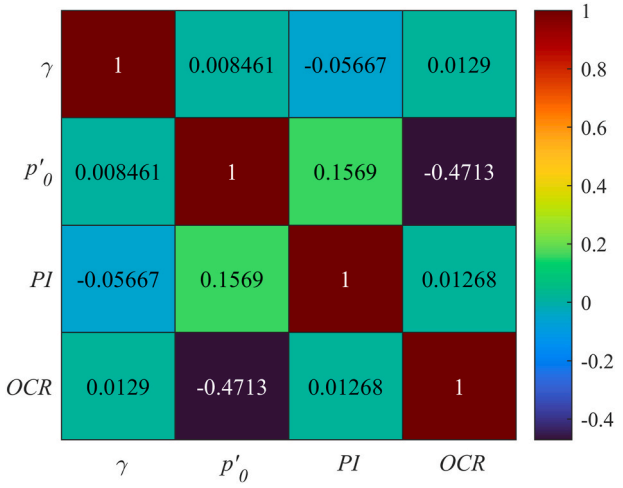

Fig. 8. Pearson correlation coefficients between the four input variables.

stress (q) is plotted against the axial strain (ε_a). The shear modulus and the damping ratio are derived from the ellipses, respectively though the secant line and the areas indicated in Fig. 5b.

2.3. Dynamic properties of the specimens investigated

Dynamic tests were conducted on cylindrical specimens with a diameter of 50 mm and height of 100 mm in RC-CTS, and a diameter of 70 mm and height of 140 mm in CTx. Following the procedures of data elaboration described in Section 2.2, 25 G-γ and D-γ curves were obtained. Only from RC and CTS results, curves of normalized shear modulus G/G_0 were computed by dividing G with respect to the small-strain shear modulus G_0. The latter cannot be captured by CTx measurements, which involve large strains. The results derived from 4 specimens retrieved from Pietrarossa dam and 1 specimen retrieved from Scanzano dam, where only CTx tests were conducted, are therefore used only for analyses in terms of G-γ and D-γ. Fig. 6 shows the G/G_0-γ and D-γ curves varying with PI, while Fig. 7 shows the same curves varying with p'_0.

The results are approximatively in line with the literature: at a given shear strain γ and with increasing PI, the normalized shear modulus increases, while damping decreases [21,27,28]. Specifically, damping decreases by increasing PI except in cases with PI<15 %. Regarding the relationship with p'_0, a direct proportionality should be seen with G/G_0 curves, while indirect proportionality with D [32,33]. This evidence from literature is more clearly observed in this experimentation in terms of D, while for G/G_0 it appears not to be so well-standardised.

3. Modelling of the experimental results based on regression techniques

3.1. Preliminary statistical analysis of the database

To predict the dynamic properties of fine-grained soils having similar characteristics of the ones analysed, models for G-γ, D-γ and G/G_0-γ curves can be derived using regression techniques. As common in regression analyses, a relationship between given inputs and target outputs must be established. In this case, the target outputs to predict were the experimental G, D and G/G_0 values (461 data points for G and D, 381 data points for G/G_0 because CTx results were not considered due to missing small-strain G_0); the inputs were: the shear strain γ related to each point of the experimental curves, PI, p'_0 (evaluated at the depths indicated in Table 1), and OCR. The latter is an increasing factor for G and G/G_0, although it is sometimes considered a secondary effect [46]. Even for D, OCR was considered as input for a uniform development of

Table 2
Statistics of the input features and output.

Input feature/output	Min	Max	Median	25th perc	75th perc
Shear strain γ (%)	3.90e-04	1.80	0.05	0.01	0.20
p'_0 (kPa)	60.00	550.00	270.00	170.00	350.00
PI (%)	10.08	46.00	27.66	16.44	31.96
OCR (−)	1.37	10.60	1.59	1.51	1.70
G (MPa)	1.00	94.78	19.00	8.38	31.40
D (%)	0.04	34.17	6.63	3.85	10.15
G/G_0 (−)	0.11	1.00	0.64	0.23	0.84

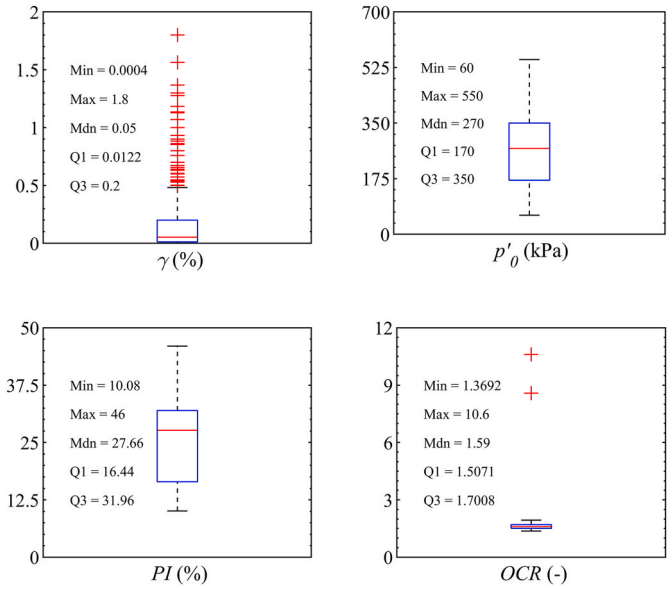

Fig. 9. Boxplots summarising the statistics of the input variables.

models, based on the same number of inputs. Since *OCR* had not been determined experimentally, we adopted the empirical formulation by Kootahi and Mayne [60] which allows for its estimation based on the index properties and the geostatic stress state. The latter formulation is briefly summarised in Appendix A.

Preliminary to model development, the Pearson correlation matrix was computed to check the potential correlation among inputs according to the reported correlation coefficients (Fig. 8). According to Mohamad et al. [61], weak correlation (correlation coefficient 0.1 ÷ 0.2) is observed between *PI* and p'_0, while a moderate correlation (correlation coefficient 0.2 ÷ 0.5) is noticed between *OCR* and p'_0. This is reasonable because *OCR* depends on p'_0. All the other inputs are not correlated with one another (correlation coefficient <0.1). Therefore, keeping the four inputs is a reasonable choice.

A statistical analysis of the dataset was then conducted by evaluating the minimum, maximum, median, and the first and third quartiles (i.e., 25th and 75th percentiles), for inputs and outputs (Table 2). The developed models will be considered valid within the ranges indicated. Boxplots representing the statistical results are also illustrated in Fig. 9. These show that data are non-normally distributed because the distribution around the median value is rarely symmetric; this qualitative observation was confirmed by performing the Anderson–Darling test. In such case, dataset normalisation is useful to improve convergency and prediction accuracy. It was done as:

$$I_{norm} = \frac{I_i - I_{min}}{I_{max} - I_{min}} \tag{2}$$

where I_i and I_{norm} indicate the raw dataset and the normalized one, respectively, while I_{min} and I_{max} are the extreme values of the dataset reported in Table 2. The database was finally partitioned into training and test dataset. The former was used to develop the model, while the latter was used to test and validate the developed model. A training/test ratio of 70:30 was used in agreement with other studies on similar topic [56–59].

3.2. Regression analysis techniques: a brief overview

Several techniques of regression analysis were adopted. They consist of finding a relationship between two or more independent variables (input) and the quantitative dependent variable (output). As mentioned above, we considered four inputs (γ, *PI*, p'_0 and *OCR*) and from them, three different models were independently developed, to predict *G*, *D* and G/G_0, respectively, considered separately as single outputs. The first regression technique adopted was the Multiple Linear Regression (MLR), based on a straight line relating inputs to the output:

$$O_{1,MLR} = b_0 + \sum_{i=1}^{4} b_i I_i \tag{3}$$

where I_i and b_i are the *i*th input and weight assign to the input, respectively, while b_0 is the bias. The MLR technique was expected to be too simple to capture the non-linearity of the output data and provide accurate results [54,62]. Therefore, regression based on ML and DL techniques was adopted to analyse if/how much the prediction accuracy of the dataset was improved through models that are more complex from a mathematical point of view. Among the existing ML/DL techniques, FeedForward Neural Network (FFN) was adopted. It is based on a network having a layered structure, made up of input, hidden and output layers. Input and output layers are made up of "nodes", while hidden layers are made up of "hidden neurons". The number of input and output nodes is defined a priori (in this study, four and one, respectively), while the topology of the hidden layers, i.e., their number and the number of hidden neurons per hidden layer, can be more or less complex depending on the complexity of the dataset to be predicted. In the following, the fundamental equations governing FFN models are provided. Single-hidden layer networks are referred to as ML technique, while multiple-hidden layer networks belong to DL techniques, due to the greater network complexity. Generally, the output of the *j*th neuron belonging to the *k*th hidden layer $z_{j,k}$ is evaluated as linear combination:

$$z_{j,k} = \sum_{i=1}^{n_{k-1}} w_{jk,i} \bullet f(z_{i,k-1}) + b_{j,k} \tag{4}$$

$z_{i,k-1}$ is the output provided by the *i*th neuron of the previous hidden layer (the *k*-1 one), the latter having n_{k-1} hidden neurons; $w_{jk,i}$ is the weight associated to $z_{i,k-1}$, and $b_{j,k}$ is the bias given by the *j*th neuron. *F* is an activation function, whose meaning will be discussed in the following. For the 1st hidden layer ($k = 1$), weights are associated directly to the four inputs and no activation function is applied. In other words, $z_{j,1}$ is evaluated as:

$$z_{j,1} = \sum_{i=1}^{4} w_{j1,i} \bullet I_i + b_{j,1} \tag{5}$$

Finally, supposing a *n*-hidden layer network, the single FFN output $O_{1,FFN}$ is given by:

$$O_{1,FFN} = \sum_{j=1}^{n_n} W_{1,j} \bullet f(z_{j,n}) + B \tag{6}$$

where n_n is the number of hidden neurons of the *n*th hidden layer, $z_{j,n}$ is the related output, and $W_{1,j}$ and *B* are the weight and bias assigned by the single neuron output to $z_{j,n}$. In turn, $z_{j,n}$ is related to the output of the previous hidden layers. Fig. 10 shows two examples of a single-hidden layer network (i.e., a network with the simplest structure) (Fig. 10a) and two-hidden layer network (Fig. 10b). The development of the network involves finding weights and biases that minimize the error

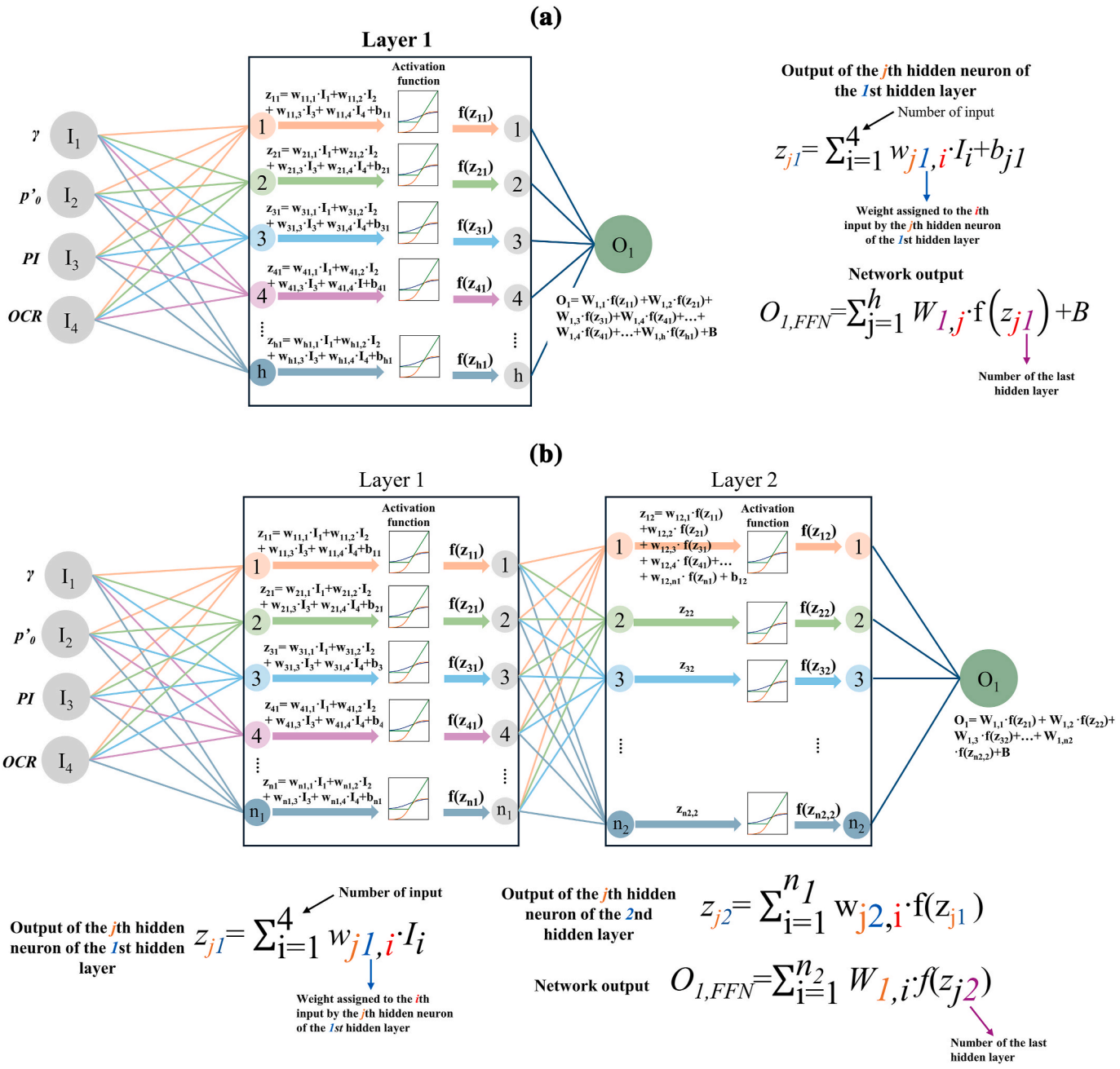

Fig. 10. Examples of a 4-input and 1-output FFN with a) one hidden layer; b) two hidden layers.

between the network's predictions and the target values. The training algorithm used is Levenberg-Marquardt, which, for the first step, considers weights initialized with the Glorot function (the default for the *fitrnet* function in MATLAB).

Eqs. (4)–(6) are not exactly a linear combination of the outputs: thanks to the activation function *f*, nonlinearity is introduced to the network, allowing it to capture even complex data patterns. Three activation functions are tested: i) Rectified Linear Unit (ReLU); ii) Sigmoid; iii) hyperbolic tangent (Tanh) whose trends are shown in Fig. 11.

The network topology providing the best performance was not known a priori. We varied the number of hidden layers from 1 to 3 (1 is for ML model; 2 and 3 for DL models), and the number of hidden neurons per layer from 1 to 50. To simplify the model development, we considered the same number of hidden neurons within each layer of multi-hidden layer models (e.g., for the three hidden layers 1-1-1, 2-2-2, …50-50-50). For each dynamic property, 150 models per activation function were realised; considering the three dynamic properties and the three tested activation functions, a total number of 1350 models were developed.

3.3. Development of hybrid FFN using Particle Swarm Optimization and genetic algorithm techniques

Hybrid FFNs were developed with weights and biases initialized using Particle Swarm Optimization (PSO) and Genetic Algorithms (GA) independently. PSO is designed to quickly identify effective starting points for training a neural network by simulating a swarm of particles searching for optimal solutions. Each particle represents a potential set of weights and biases and is evaluated based on its ability to predict target values. Performance is measured using a fitness function, such as Mean Squared Error (MSE). The adjustment of weights and biases is influenced by two key factors: the best position found by the individual

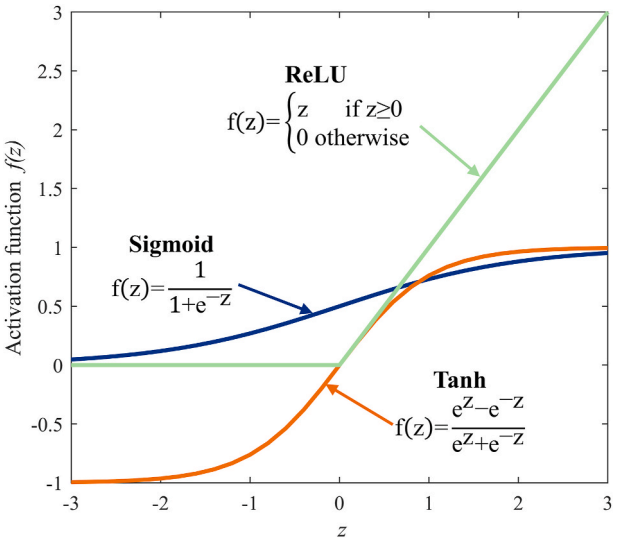

Fig. 11. Activation functions: ReLU, sigmoid and hyperbolic tangent (Tanh).

particle (i.e., its most effective set of weights and biases) and the best position found by the entire swarm (i.e., the most effective set of weights and biases discovered by any particle in the swarm). Particles move through the weight and bias space, converging on optimal or near-optimal solutions by adjusting their positions based on both personal experience and collective knowledge. This iterative process enhances convergence speed during training and reduces the likelihood of being trapped in local minima. A detailed description of the PSO algorithm can be found in Refs. [63–65].

In parallel, Genetic Algorithms (GA) were employed as an alternative method for initializing weights and biases. Inspired by evolution and natural selection principles, GA begins with a randomly generated population of candidate solutions, representing initial weights and biases. The algorithm then iterates through processes of selection, crossover, and mutation. Selection favors individuals with higher fitness scores, representing better solutions. Pairs of selected individuals are recombined through crossover, producing offspring with mixed characteristics. Mutation introduces small random changes to some individuals, maintaining population diversity and allowing exploration of a broader search space. These processes collectively improve the quality of weights and biases over time. The GA approach is described in detail in literature [66,67].

By using both PSO and GA for initialization independently, we aimed

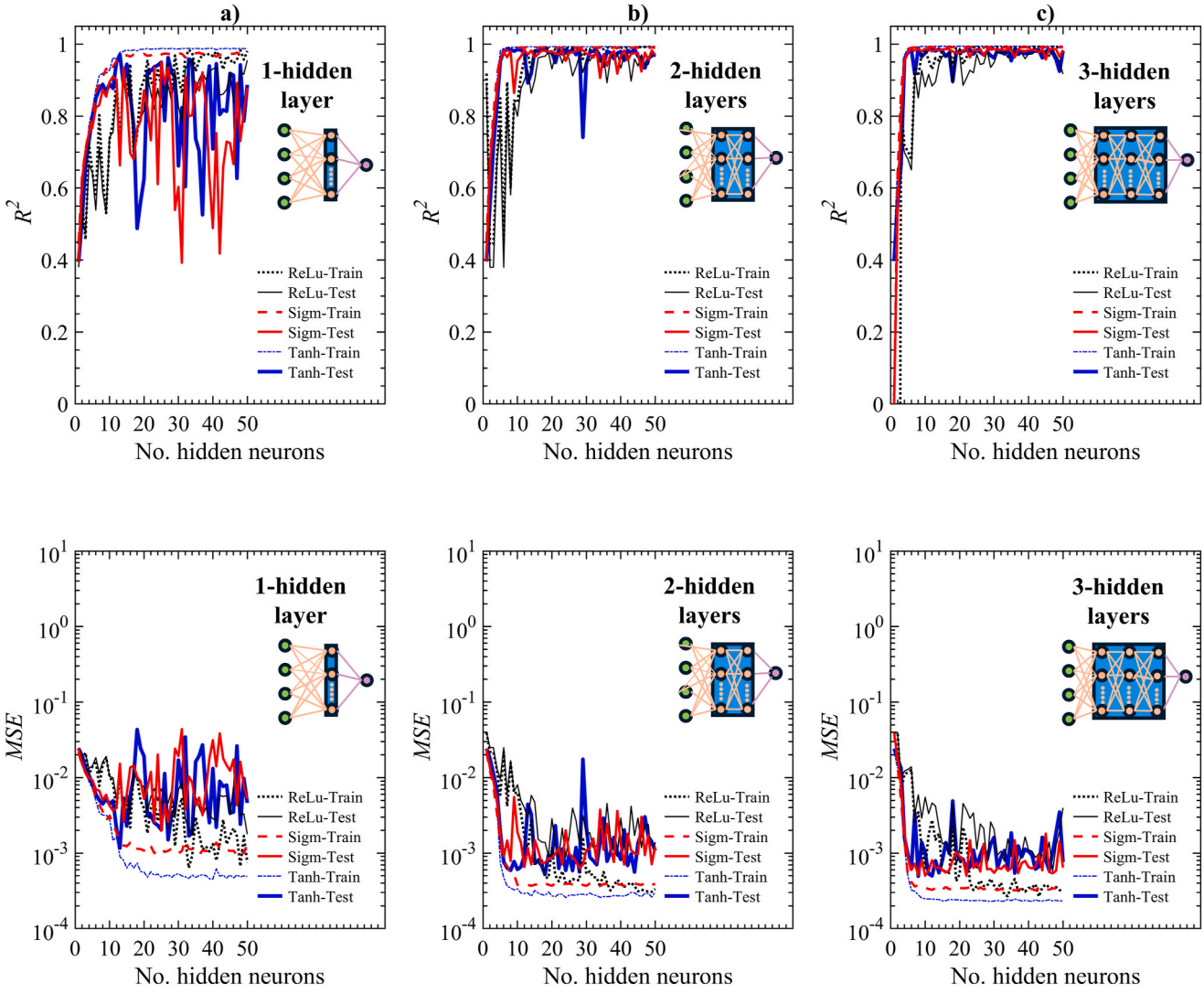

Fig. 12. Development of *G-γ* model. Coefficient of correlation R^2 and Mean Squared Error *MSE* derived with a) single-, b) two-, and c) three-hidden layer network and number of neurons per hidden layer varying 1 ÷ 50.

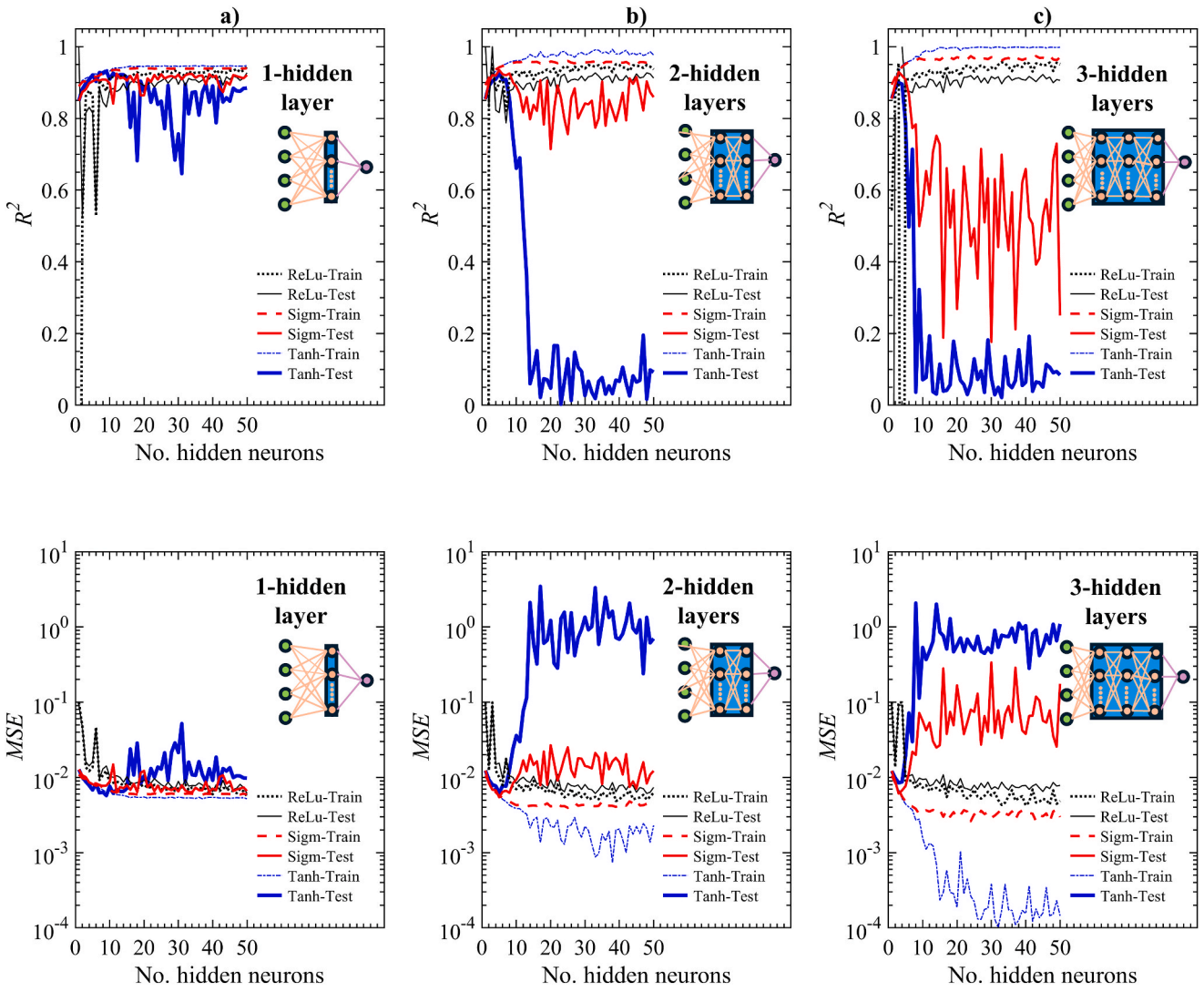

Fig. 13. Development of G/G_0-γ model. Coefficient of correlation R^2 and Mean Squared Error *MSE* derived with a) single-, b) two-, and c) three-hidden layer network and number of neurons per hidden layer varying 1 ÷ 50.

to compare the effectiveness of these algorithms in providing high-quality starting points for FFN training. In MATLAB, the functions "*ga*" and "*particleswarm*" from the Global Optimization Toolbox were utilized for these optimization procedures. Subsequently, the hybrid FFN regression was conducted using the "*feedforwardnet*" function from the Deep Learning Toolbox, with user-defined initial weights and biases derived from these optimization methods.

3.4. Metrics for performance evaluation

By changing the FFN topology, as well as the activation function, the network performance will differ. We are interested in finding the best configuration, in terms of number of hidden layers, number of neurons per hidden layer, and activation function, providing the greatest accuracy. Accuracy is evaluated through the coefficient of correlation R^2 and the Mean Squared Error *MSE*, defined as:

$$R^2 = 1 - \frac{\sum_{i=1}^{N} (e_i - p_i)^2}{\sum_{i=1}^{N} (e_i - \underline{e})^2} \tag{7a}$$

$$MSE = \frac{\sum_{i=1}^{N} (e_i - p_i)^2}{N} \tag{7b}$$

where e_i is the ith experimental value, p_i is the corresponding predicted value, N is the total number of observations/predictions and $\underline{e}$ is the average of the experimental values. A good model is defined as one providing large R^2 and small *MSE*, especially with the test dataset.

4. Results

4.1. Calibration of the FFN model

R^2 and *MSE* varying with the number of hidden layers (1 ÷ 3) and number of neurons per hidden layer (1 ÷ 50) were evaluated for the G-γ model (Fig. 12), for the G/G_0-γ model (Fig. 13) and for the D-γ model (Fig. 14). Values derived from training and test dataset are reported, with dashed and continuous line, respectively. Fig. 12 shows the results related to G-γ; regardless of the activation function, R^2 and *MSE* evaluated with the training dataset are respectively greater and smaller than those computed with the test dataset. This is logical and correct because the training dataset used to develop the model comprises 70 % of the database. By increasing the number of hidden layers, R^2 increases, and

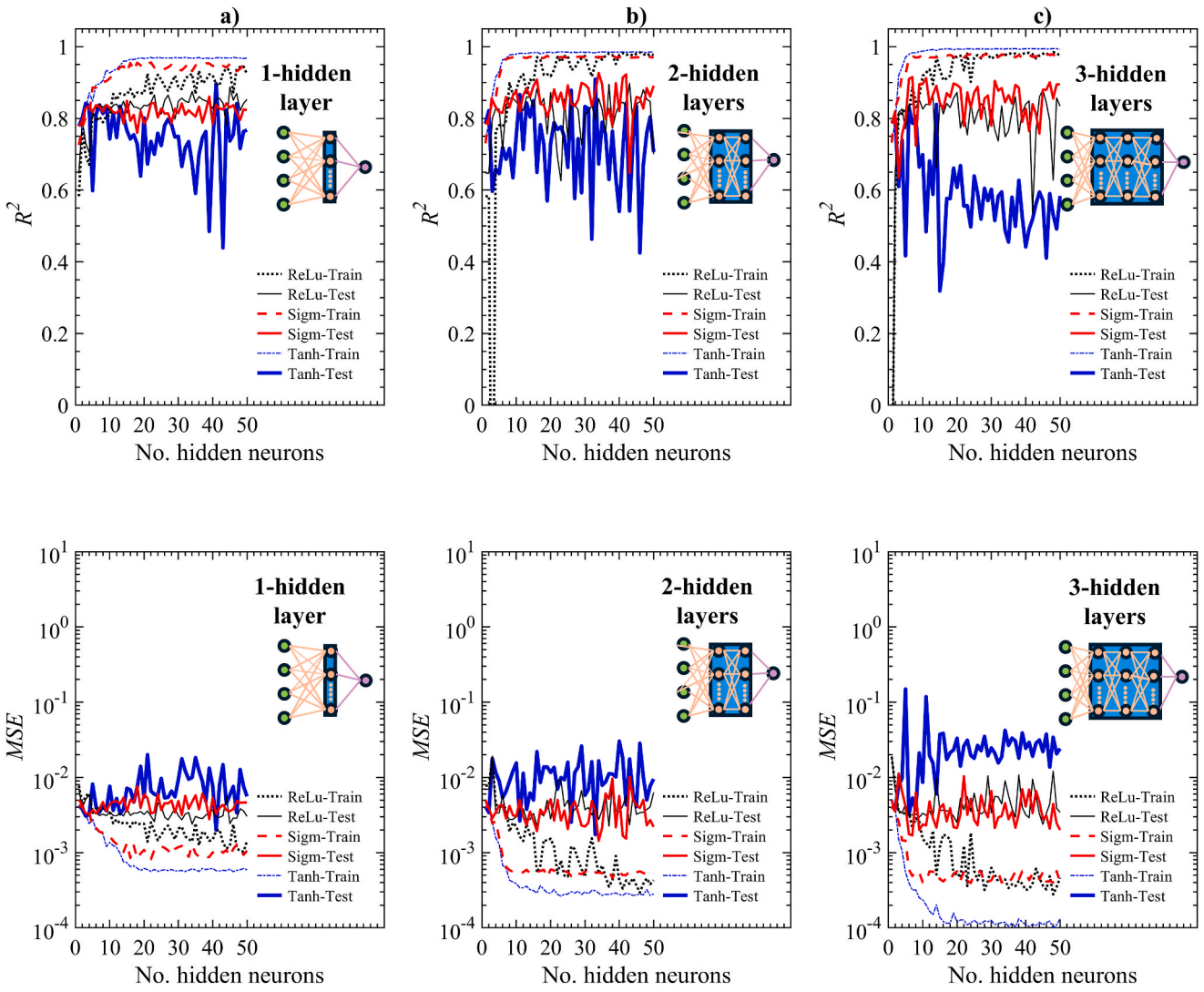

Fig. 14. Development of *D-γ* model. Coefficient of correlation R^2 and Mean Squared Error *MSE* derived with a) single-, b) two-, and c) three-hidden layer network and number of neurons per hidden layer varying 1 ÷ 50.

Table 3
Coefficients of correlation R^2 (evaluated on training and test dataset) and Mean Squared Error *MSE* (evaluated on test dataset) related to the best FFN models predicting the shear modulus *G*, one per activation function and number of hidden layers. *m* indicates the number of hidden neurons per hidden layer at which R^2_{test} is maximum.

	Model											
	Single layer				Double layer				Triple layer			
Activation Function	*m*	R^2_{test}	MSE_{test}	$R^2_{training}$	*m*	R^2_{test}	MSE_{test}	$R^2_{training}$	*m*	R^2_{test}	MSE_{test}	$R^2_{training}$
ReLU	34	0.9563	0.0017	0.9765	49	0.9800	0.0008	0.9922	47	0.9855	0.0006	0.9913
Sigmoid	25	0.9504	0.0020	0.9713	28	0.9844	0.0006	0.9899	22	0.9875	0.0005	0.9913
Tanh	13	0.9711	0.0012	0.9772	18	0.9869	0.0005	0.9930	8	0.9878	0.0005	0.9929

Table 4
Coefficients of correlation R^2 (evaluated on training and test dataset) and Mean Squared Error *MSE* (evaluated on test dataset) related to the best FFN models predicting the normalized shear modulus G/G_0, one per activation function and number of hidden layers. *m* indicates the number of hidden neurons per hidden layer at which R^2_{test} is maximum.

	Model											
	Single layer				Double layer				Triple layer			
Activation Function	*m*	R^2_{test}	MSE_{test}	$R^2_{training}$	*m*	R^2_{test}	MSE_{test}	$R^2_{training}$	*m*	R^2_{test}	MSE_{test}	$R^2_{training}$
ReLU	50	0.9268	0.0061	0.9435	48	0.9271	0.0061	0.9488	45	0.9223	0.0065	0.9477
Sigmoid	12	0.9249	0.0063	0.9353	8	0.9252	0.0062	0.9517	6	0.8659	0.0115	0.9578
Tanh	9	0.9316	0.0057	0.9367	7	0.9082	0.0077	0.9518	7	0.7139	0.0298	0.9627

Table 5
Coefficients of correlation R^2 (evaluated on training and test dataset) and Mean Squared Error *MSE* (evaluated on test dataset) related to the best FFN models predicting the damping ratio *D*, one per activation function and number of hidden layers. *m* indicates the number of hidden neurons per hidden layer at which R^2_{test} is maximum.

	Model											
	Single layer				Double layer				Triple layer			
Activation Function	*m*	R^2_{test}	MSE_{test}	$R^2_{training}$	*m*	R^2_{test}	MSE_{test}	$R^2_{training}$	*m*	R^2_{test}	MSE_{test}	$R^2_{training}$
ReLU	45	0.8870	0.0024	0.9340	43	0.8980	0.0023	0.9793	45	0.8795	0.0024	0.9804
Sigmoid	39	0.8607	0.0028	0.9531	34	0.9268	0.0014	0.9708	7	0.9153	0.0017	0.9738
Tanh	41	0.8967	0.0020	0.9692	33	0.9094	0.0017	0.9832	14	0.8389	0.0060	0.9892

Table 6
Final FFN topologies providing the best prediction with simpler network (suggested for practitioners) and with more complex network (suggested for advanced users). The first and last number in the topology indicate respectively the input and output number (four and one in our problem).

Predicted Output	Practitioners			Advanced users		
	Topology	Activation function	R^2_{test}	Topology	Activation function	R^2_{test}
Shear modulus *G*	4-13-1	Tanh	0.97	4-8-8-8-1	Tanh	0.99
Normalized shear modulus G/G_0	4-9-1	Tanh	0.93	4-9-1	Tanh	0.93
Damping ratio *D*	4-15-1	Sigmoid	0.85	4-34-34-1	Sigmoid	0.93

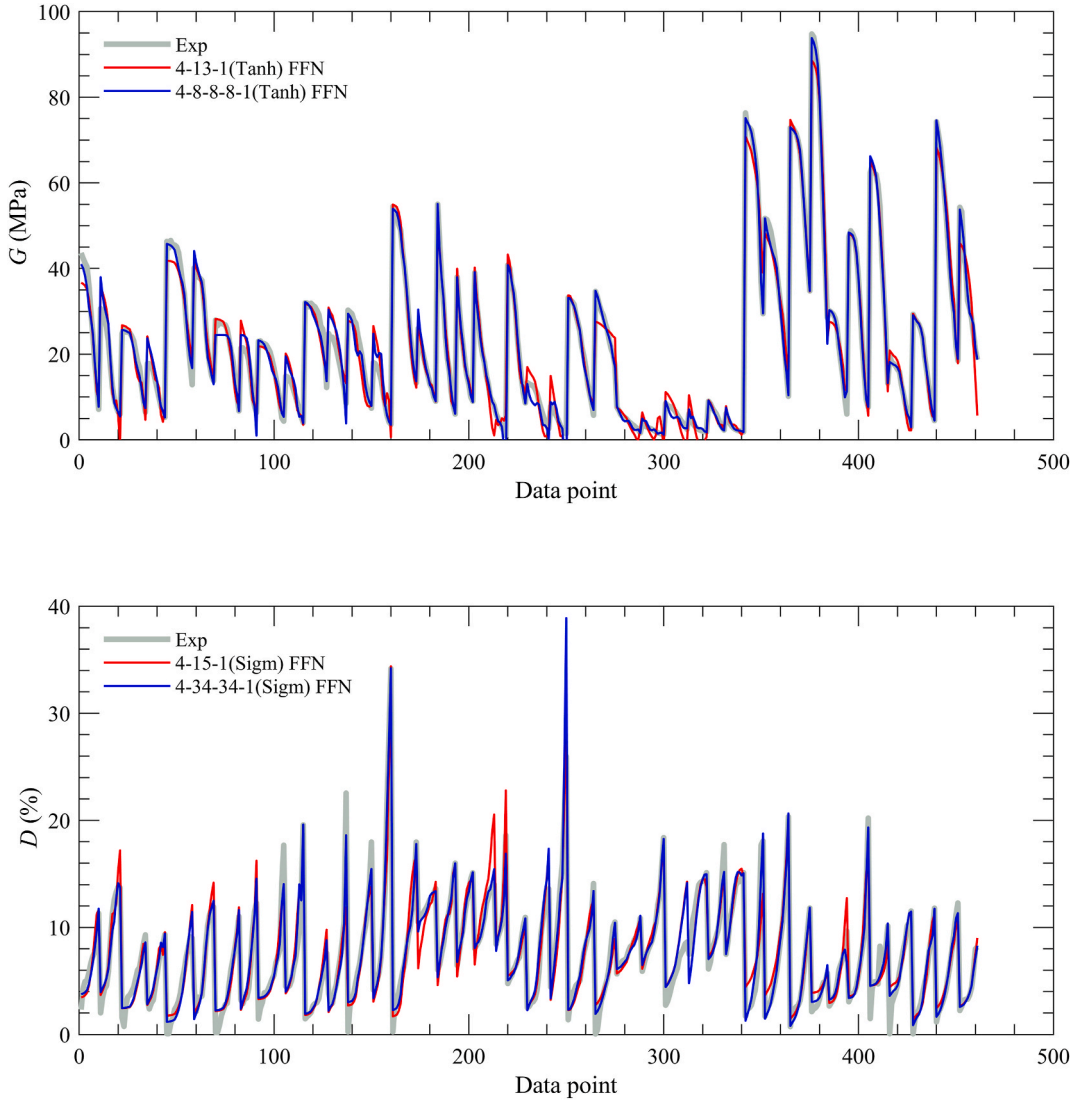

Fig. 15. Comparison of the predictions derived through FFN models with simple or complex structure.

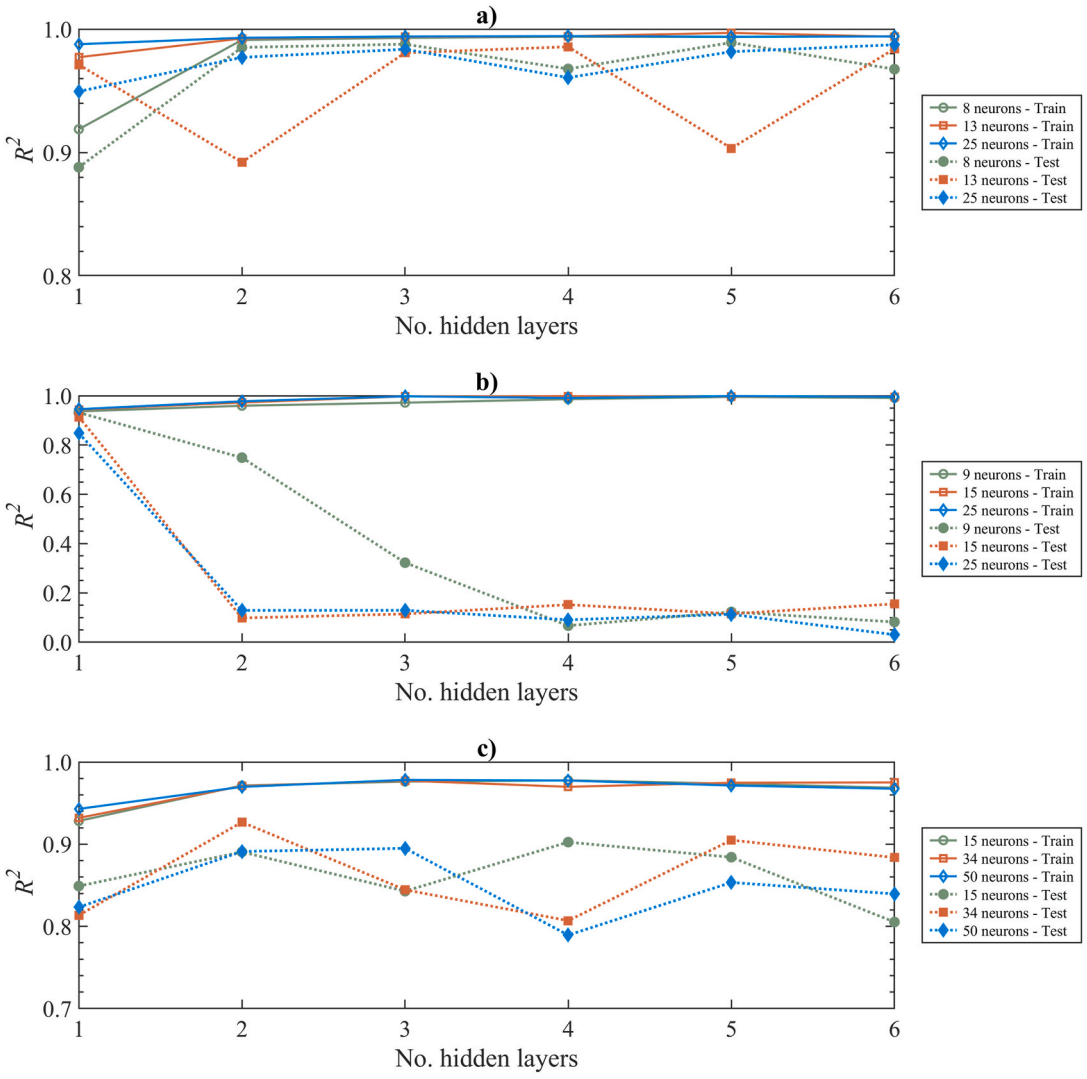

Fig. 16. Coefficient of correlation R^2 as a function of the number of FFN hidden layers for the training (solid lines) and test (dashed lines) datasets in the a) *G*, b) G/G_0, and c) *D* models. Each subplot compares different neuron counts per hidden layer.

only a slight difference can be noticed in the results. In terms of *MSE*, the behaviour is less clear: a reduction in error is observed by increasing the number of hidden layers, but it is not as marked when going from 2 to 3 hidden layers. By increasing the number of hidden neurons, a more stable behaviour was expected, but this trend is not seen in any configuration. Regarding the performance of the three activation functions, we can state that Tanh and Sigmoid provide better accuracy than ReLU. Table 3 reports the number of hidden neuron *m* at which the coefficient of correlation evaluated on the test dataset R^2_{test} is maximum, together with the related mean squared error MSE_{test}. $R^2_{training}$ of models with *m* hidden neurons is also reported. For all cases, R^2 is greater than 0.95, indicating good accuracy. The greatest R^2_{test}, equal to 0.9878, is found through the 4-8-8-8-1 network and Tanh activation function. Very good accuracy is observed when applying such activation function even on a single hidden layer network ($R^2_{test} = 0.9711$ with 4–13-1 topology). The adoption of a model showing a slightly smaller R^2_{test} (only 2 % less) but having a simpler topology could be an interesting solution for practitioners.

Fig. 13 presents interesting results for G/G_0 model. The Tanh activation function provides the most accurate results with the training dataset regardless of the number of hidden layers; moreover, the accuracy increases with increasing complexity of the network topology. However, on the test dataset, the model accuracy with networks having more than 10 neurons is drastically reduced, with the coefficient of correlation R^2_{test} going from around 0.9 to 0.1 and MSE_{test} from 10^{-2} to more than 1, for both two- and three-hidden layer models. With the sigmoid activation function, a similar but less pronounced behaviour is observed. Despite the unexpected behaviour observed with DL models, ML models with Tanh activation function are more stable, showing comparable R^2_{test} and R^2_{train} within 10 hidden neurons. Table 4 summarises the properties of the models providing the best R^2_{test}. As the final and best choice for G/G_0, the model 4-9-1 with Tanh as activation function can be selected; this can be adopted even by practitioners thanks to its simple structure.

From the results related to the D-γ model (Fig. 14), the coefficient of correlation R^2_{train} obtained with the Tanh activation function tends to an asymptotic value after a certain number of hidden neurons m_{crit}; specifically, m_{crit} diminishes when increasing the network complexity in terms of number of hidden layers. With the test dataset, there is a narrow range of neurons in which R^2_{test} decreases and MSE_{test} increases despite the increasing complexity of the network, as for the G/G_0 model. However, for the D-γ model, there is also a very narrow neuron range in which R^2_{test} is comparable to R^2_{train} (around 0.8). This occurs up to about 5 neurons, which may not be enough to properly develop a DL model able to capture the complexity of data related to damping. Table 5 reports the number of hidden neurons *m* at which the coefficient of correlation

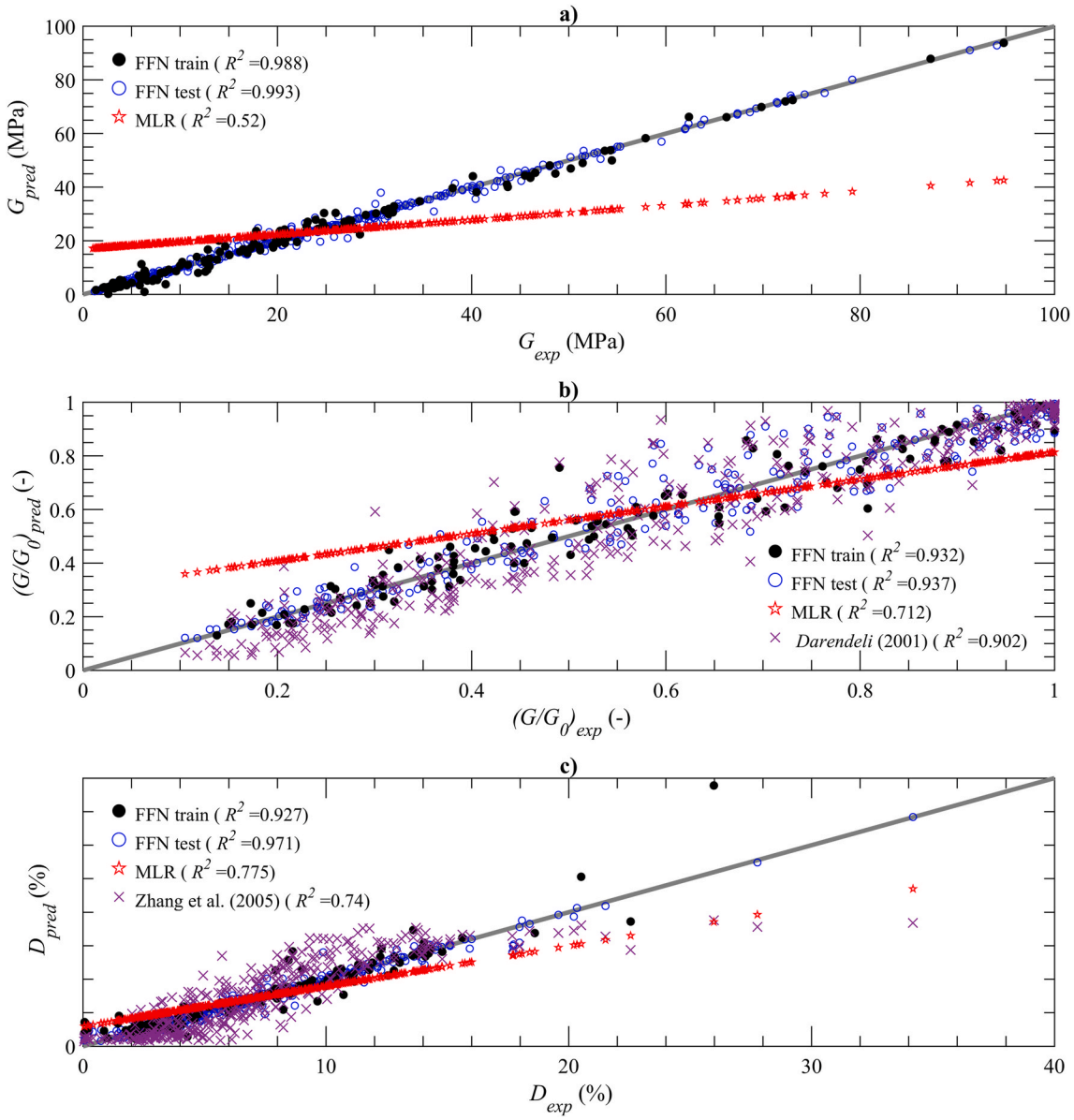

Fig. 17. Experimental data vs predictions derived through FFN and MLR regression, and other existing empirical methods for G/G_0 [40] and D [29].

Table 7
Comparison of R^2 values for both the training and test datasets, alongside training time (t_{train}) and inference time (t_{infer}) for FFNs with simple topologies. The performance of FFNs initialized with weights and biases using the Glorot function (MATLAB's default setting) against those initialized through optimization algorithms, such as Particle Swarm Optimization (PSO) and Genetic Algorithm (GA), is contrasted. This comparison provides insights into the effectiveness and efficiency of different initialization methods.

Model	G (4-13-1 Tanh)			G/G_0 (4-9-1 Tanh)			D (4-15-1 Sigmoid)		
Weights/Biases initialization	Glorot	PSO	GA	Glorot	PSO	GA	Glorot	PSO	GA
R^2_{train}	0.9772	0.9859	0.9840	0.9367	0.9325	0.9383	0.9067	0.9448	0.9660
R^2_{test}	0.9711	0.9625	0.9500	0.9316	0.9266	0.8847	0.8510	0.7049	0.5185
t_{train} (s)	15.948	21.554	36.438	7.5447	11.654	9.8681	13.398	36.713	50.836
t_{infer} (s)	0.0018	0.012	0.2330	0.0011	0.0086	0.0078	0.0167	0.2295	0.2315

evaluated on the test dataset R^2_{test} is maximum, the related Mean Squared Error MSE_{test}, and the $R^2_{training}$ of models with m hidden neurons. For the single hidden layer network with the sigmoid activation function, although the absolute maximum value of R^2_{test} is observed at 39 hidden neurons, there is a local maximum with 15 neurons and a comparable R^2_{test} (around 0.85). Results obtained through ReLU and sigmoid activation functions are quite similar. Since the sigmoid provides a good R^2_{train} with asymptotic trend, it could be considered the best activation function to predict damping. The simple model (topology 4-15-1) could be the best choice for practitioners, while 4-34-34-1 can be considered for advanced users.

Based on the data analysed, we summarise in Table 6 the topologies that can be the best choice for practitioners (best accuracy with simpler topology) or advanced users (best accuracy with possibly more complex

Table 8
Summary of borehole locations, mean sampling depths, plasticity index *PI*, USCS classification, confining pressure p'_0, and overconsolidation ratio *OCR* for the tests in the external dataset provided by Facciorusso [68]. The asterisk (*) indicates that *OCR* was evaluated using the method proposed by Kootahi and Mayne [60].

Location	Borehole label	Depth (m)	*PI* (%)	USCS classification	p'_0 (kPa)	*OCR*
Fabriano (Marche region)	S61	8.75	32	CH	150	1.9
Città di Castello (Umbria region)	S45	3.30	16	CL	120	2.3
Terni – Rieti (Umbria region-Lazio region)	S31	9.30	33	CH	90	1.61*

topology). Appendix B reports weights and bias of the single-hidden layer models, to allow practitioners' usage following the description and Eqs. (4)–(6) reported in Section 3.2.

The 4-9-1 network with Tanh activation function is observed to provide the most accurate predictions of the normalized shear modulus, even in comparison with more complex models. Fig. 15 shows the predictions on the whole dataset (test + training) of *G*- and *D*-γ curves, derived through simple and more complex models, to analyse what error could be committed by practitioners when adopting simple FFN topologies. Overall, models based on DL (multiple hidden layer networks) provide more accurate predictions; however, the comparison demonstrates that single-hidden layer networks allow for the development of ML models that are more than acceptable.

To explore whether network complexity correlates with accuracy, neural networks with hidden layers ranging from 1 to 6 were developed. For each network configuration, three different numbers of hidden neurons were tested, including those reported in Table 6. The activation functions used were Tanh for the *G* and G/G_0 models, and Sigmoid for the *D* model. For each network, with a fixed number of neurons, the R^2 values calculated on the training dataset generally improved, showing an asymptotic trend starting from 2 hidden layers, and in some cases, even from a single layer (Fig. 16). This indicates that while more complex networks may have the potential to learn better, good performance can also be achieved with simpler networks, particularly if the dataset is not highly complex. In the *G* model, the R^2 values on the test dataset were generally comparable to those on the training dataset (Fig. 16a). No significant improvement in performance was observed with increased model complexity, and a single-layer network with 13 neurons proved to be quite effective. In the G/G_0 model, an interesting trend was noted (Fig. 16b). Although the training R^2 values exhibited an asymptotic trend starting from 2 hidden layers, the test R^2 values showed a lower horizontal asymptote, with a significant drop in performance (R^2 less than 0.2) despite increased network complexity. This suggests potential overfitting, as the dataset may be too simple for the more complex networks. The simpler model with 9 neurons showed a horizontal asymptote starting from 4 hidden layers. For the *D* model, prediction accuracy on the test dataset displayed fluctuating and irregular behaviour, with no clear horizontal asymptote (Fig. 16c). The result once again confirms that the previously chosen simple models show acceptable performance.

4.2. Experimental results vs predictions derived through existing empirical methods and the developed FFN and MLR models

The experimental data are here compared with predictions derived through FFN and the topology above defined as "for advanced users", and the MLR. For G/G_0 and *D*, values calculated through some common methods provided by literature are also reported. We have adopted Darendeli [40] and Zhang et al. [29] respectively for G/G_0 and *D* predictions, by applying the formulations and modelling parameters discussed in Appendix C. The comparison is shown in Fig. 17.

In terms of shear modulus (Fig. 17a), FFN applied on both training and test datasets appears to perform superior, adhering more closely to the line of equality (grey), particularly for *G* values higher than about 30 MPa. MLR tends to underestimate *G*, especially at higher values. Regarding G/G_0 (Fig. 17b), the FFN is still outperforming in approximating the line of equality. Predictions through Darendeli's method exhibits greater dispersion, particularly for intermediate values. Finally, in terms of damping predictions, the FFN models appears to slightly outperform the MLR, adhering more closely to the line of equality; even in this case, data derived through an existing empirical method [29] shows greater dispersion, with a tendency to underestimate.

4.3. Hybrid FFN

As mentioned in Section 3.3, two optimization algorithms, PSO and GA, were used to initialize the weights and biases of the FFN. The best topologies and activation functions for each dynamic property, as reported in Table 6, were applied. A comparison was made between the prediction accuracy, training time, and inference time obtained with MATLAB's default *fitrnet* settings (which use Glorot initialization) and the results after applying the two optimization algorithms. Table 7 presents the R^2 values for both the training and test datasets, as well as the training time t_{train} and inference time t_{infer} (i.e., time required for new predictions).

The use of the PSO and GA algorithms generally led to an increase in R^2_{train} (except for PSO in the G/G_0 model). However, the prediction accuracy on the test dataset was still better when weights were initialized using the Glorot algorithm. Training times were longer for PSO- and GA-based FFNs, as both algorithms encounter slower convergence issues. Additionally, inference time was lower with Glorot initialization, indicating that this configuration allows the FFN to generate predictions more quickly. Consequently, it was decided to proceed with weights initialized using Glorot.

4.4. Prediction on external dataset

A newly constructed dataset was used to further validate the developed FFN models. It includes the results of three RC tests on fine-grained soil samples, extracted from the Italian Clay Archive provided by Facciorusso [68]. The tests were carried out in the geotechnical laboratory of the Civil and Environmental Engineering Department at the University of Florence, using samples collected from different regions in Italy, outside of Sicily. Table 8 summarises locations, sampling depths, USCS classifications, *PI*, p'_0, and OCR.

The three best-performing FFN models, with topologies and activation functions listed in Table 6, were applied to the entire dataset, normalized according to the extremes of the previous training dataset (Table 2). Fig. 18 presents a comparison between the experimental results and those predicted by the FFN models. For *G*, the predictions are acceptable, though not consistently excellent, with *MSE* values ranging from 126 to 242. The predictions for G/G_0 are significantly better, with *MSE* consistently below 0.02. Finally, the predictions for *D* are fairly accurate for small damping values, but for higher values, damping tends to be underestimated, with *MSE* ranging from 3 to 12.

5. Discussion

RC, CTS and CTx tests performed on 25 specimens of fine-grained soils retrieved in Sicily have revealed quite standard variations of the normalized shear modulus and G/G_0 the damping ratio *D* with respect to the plasticity index *PI* and the confining pressure p'_0: at a given shear

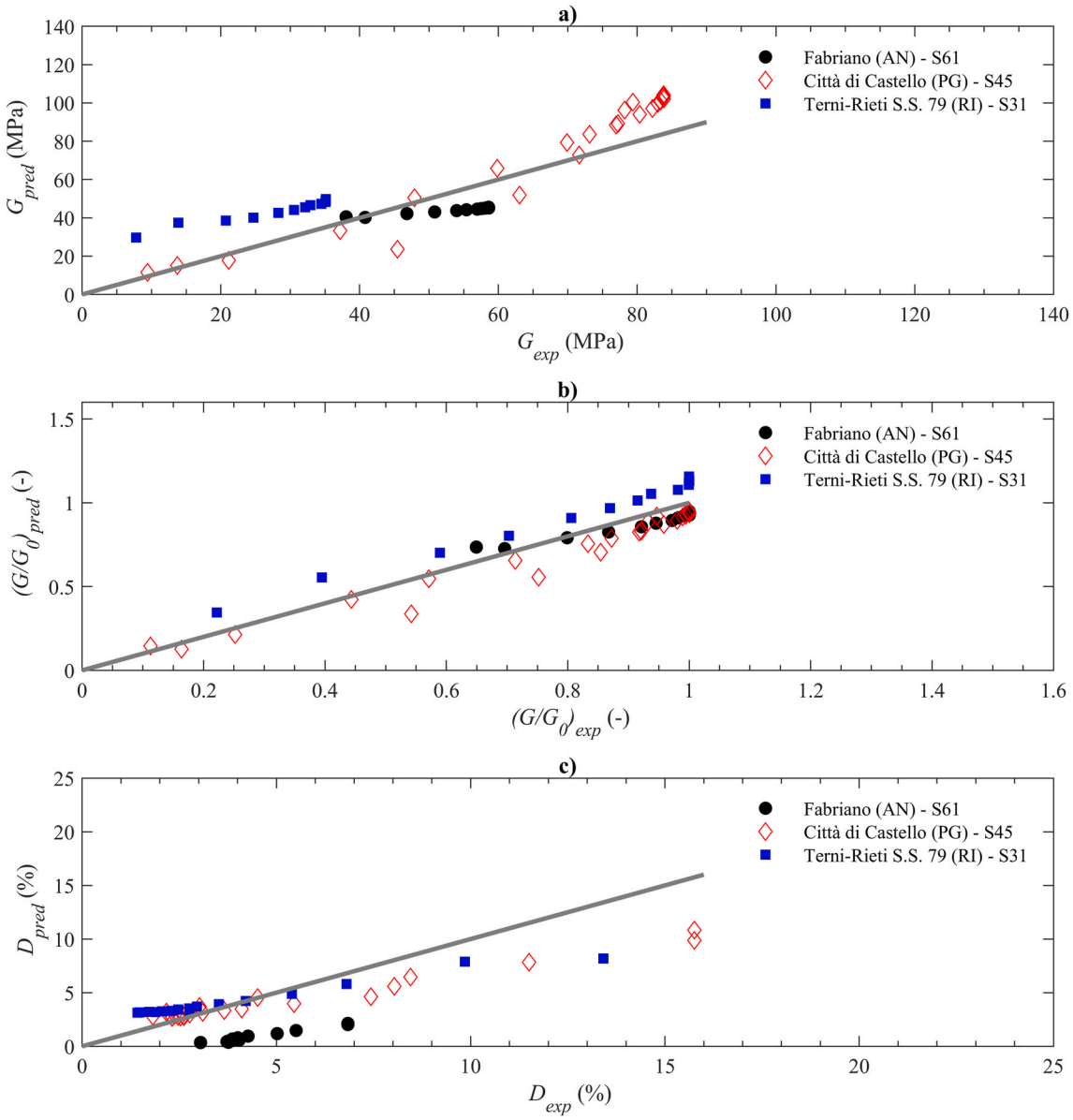

Fig. 18. Comparison between predicted and experimental values for three dynamic soil properties: a) shear modulus (G), b) normalized shear modulus (G/G_0), and c) damping ratio (D). The predictions were based on experimental data extracted from the Italian Clay Archive [68] related to three different borehole locations: Fabriano (Marche region, black circles), Città di Castello (Umbria region, red diamonds), and Terni-Rieti (Umbria and Lazio regions, blue squares). The solid grey line represents the 1:1 line, indicating perfect agreement between predicted and experimental values.

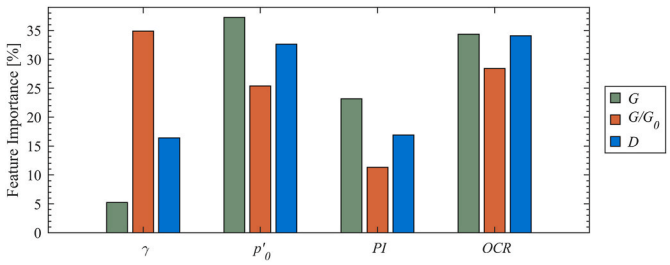

Fig. 19. Feature importance analysis for the prediction of three dynamic soil properties: shear modulus (G), normalized shear modulus (G/G_0), and damping ratio (D), based on the simple topologies reported in Table 6. The importance of four input features is shown: shear strain (γ), confining pressure (p'_0), plasticity index (PI), and overconsolidation ratio (OCR).

strain, G/G_0 increases and D decreases with both PI and p'_0. These findings are consistent with established studies [21,27–30] and recent research [31,46]. Any deviations from these standard trends may arise from the simultaneous consideration of PI and p'_0 in our results.

Empirical formulations, such as those proposed by Darendeli [40] or Zhang et al. 29, are based on modelling parameters that may not be unique even within the same country and for the same soil type. For instance, using Darendeli's formulation with modelling parameters specifically calibrated, Ciancimino et al. [46] achieved an R^2 value of 0.943 when predicting G/G_0 of fine-grained soils from central Italy. In contrast, with the same parameters, the coefficient of correlation for the results of this study is 0.904. Furthermore, other researchers have demonstrated that existing empirical formulations often require improvement or specific calibration of parameters to provide accurate predictions [43–45,58].

For developing new empirical models, regression techniques can be utilized. This study indicates that multiple linear regression is

inadequate for capturing the nonlinearities in the dynamic properties of the soil. This is consistent with findings from other studies [54,62]. A more sophisticated approach, such as Feedforward Neural Networks (FFN), demonstrates better performance in predicting complex data. Among activation functions, the hyperbolic tangent (Tanh) generally yields the best results, except for very complex data like the damping ratio, where the sigmoid function performs better. Similar results were observed by Khanlari et al. [69] and Charles et al. [59].

A very complex neural network, characterised by a large number of hidden layers and neurons, is not always optimal, as also shown by Merayo et al. [70]. On predicting G/G_0, which has less differentiation in data, complex architectures tend to overfit: while the correlation coefficient is high for the training dataset, it is considerably lower for the test dataset. In contrast, for G (non-normalized), which depends on small-strain values G_0, the network's prediction ability improves with an increasing number of hidden layers, even for the test dataset. Nevertheless, simpler models are more practical for practitioners. For the G-γ model, a topology with only 13 hidden neurons provides good accuracy, aligning with other studies on this topic [50,53,58]. For damping prediction, a network with two hidden layers and 34 neurons per layer performs well. Although this topology might seem complex, it is less so compared to other studies with more intricate structures for damping prediction [55]. For practical applications, a simpler structure with just 15 neurons offers acceptable prediction accuracy ($R^2 = 0.85$).

To determine how each feature contributes to the developed models, we used the permutation method to assess feature importance. This method involves randomly shuffling the values of each feature and measuring the resulting impact on the model's performance, specifically in terms of *MSE*. Fig. 19 shows the feature importance for the simplest models with the optimal topology discussed earlier. Generally, the features have a similar influence on performance, with importance values ranging from 15 % to 30 %. This indicates that the models are well-balanced, with no single feature dominating the predictions. However, the lower importance of γ in the G model suggests that it has a smaller role in influencing the predictions compared to other features. This limited impact requires further investigation.

The experimental results presented can be applied to predict the dynamic properties of fine-grained soils with $PI = 10.08 \div 46$ %, $OCR = 1.37 \div 10.6$, subjected to the confining pressure $p'_0 = 60 \div 550$ kPa. Strain-dependent G, G/G_0 and D can be evaluated for the strain range $\gamma = 3.9{\cdot}10^{-4} \div 1.8$ %. Knowing γ, PI, OCR and p'_0, practitioners can use the developed FFN models through simple calculation tools (e.g., Excel or manual calculations), by applying the weights and biases provided in Appendix B and using the single-hidden layer networks with the specified structure. Advanced users can also use the multiple hidden layer network with the MATLAB function "predict" by inputting the four parameters in a matrix.

It is important to note that while our models, validated with a new dataset from the Italian Clay Archive, generally perform well, they were developed using only Sicilian samples and exhibit variability when applied to a more diverse dataset from other regions in Italy. Predictions for G are acceptable but inconsistent, whereas predictions for G/G_0 are notably better. However, the models tend to underestimate damping at higher values when predicting D. These limitations highlight the need for future research to train models on a wider range of soil conditions to improve accuracy and robustness. To achieve this, FFNs could be trained with more extensive and diverse datasets, which would enhance their predictive capability across various fine-grained soils without relying on site-specific adjustments. Additionally, evaluating other machine learning techniques such as Random Forest, Support Vector Machines, or Gradient Boosting could provide further insights into their comparative accuracy with FFNs, guiding future research directions.

6. Conclusions

This study investigated the dynamic properties of fine-grained soils from Sicily through extensive laboratory testing and developed predictive models using various regression techniques. Our results regarding the variations in G/G_0 and D with PI and p'_0 are consistent with established literature. FFN outperformed MLR and existing empirical formulations in predicting strain-dependent soil properties. Notably, simpler FFN structures often yielded sufficiently accurate predictions for practical applications. The developed models are applicable to fine-grained soils with PI ranging from 10.08 % to 46 %, OCR between 1.37 and 10.6, and p'_0 from 60 to 550 kPa, across strain ranges from $3.9{\cdot}10^{-4}$ to 1.8 %. These models are crucial for site response analyses and dynamic soil-structure interaction studies. However, their accuracy is expected to be higher for soils similar to those studied, underscoring the site-specific nature of soil behaviour. Future research should focus on developing more generalized FFN models by incorporating data from a variety of geological settings and exploring additional machine learning techniques. This study makes a significant contribution to understanding fine-grained soil behaviour under dynamic loading and offers practical, AI-based tools for geotechnical engineering applications.

Funding

This research did not receive any specific grant from funding agencies in the public, commercial, or not-for-profit sectors.

CRediT authorship contribution statement

Michele Placido Antonio Gatto: Writing – review & editing, Writing – original draft, Visualization, Software, Methodology, Investigation, Formal analysis, Conceptualization. **Francesco Castelli:** Supervision, Project administration, Investigation, Funding acquisition, Formal analysis. **Valentina Lentini:** Writing – review & editing, Supervision, Investigation, Formal analysis. **Lorella Montrasio:** Writing – review & editing, Supervision, Methodology, Formal analysis, Conceptualization.

Declaration of competing interest

The authors declare that they have no known competing financial interests or personal relationships that could have appeared to influence the work reported in this paper.

Acknowledgements

This study was carried out within the RETURN Extended Partnership and received funding from the European Union Next-GenerationEU (National Recovery and Resilience Plan – PNRR, Mission 4, Component 2, Investment 1.3 – D.D. 1243 August 2, 2022, PE0000005).

Appendix A

This appendix briefly summarises the empirical formulation proposed by Kootahi and Mayne [60] for estimating the preconsolidation stress σ'_p and consequently the overconsolidation ratio OCR, defined as σ'_p/σ'_{v0}, where σ'_{v0} represents the effective vertical stress under geostatic conditions. The formulation was derived from a dataset comprising laboratory test results on 120 fine-grained soil specimens collected from 59 sites worldwide (Canada, China, Iran, Ireland, Italy, Japan, the Pacific Ocean, Singapore. Thailand, and the United States of America). The dataset includes

information on σ'_p, obtained from Oedometer tests, σ'_{v0}, the void index in natural conditions e_n, natural water content w_n and Atterberg limits (liquid limit w_L and plastic limit w_P). The authors demonstrated their formulation accurately predicts σ'_p for both the model-building dataset ($R^2 = 0.89$) and the validation dataset ($R^2 = 0.83$). The method relies on a discriminant function *DS,* expressed as:

$$DS = 5.152 \bullet \log\left(\frac{\sigma'_{v0}}{p_a}\right) - 0.061 \bullet w_L - 0.093 \bullet w_P + 6.219 \bullet e_n \quad \text{(A1)}$$

where p_a is the atmospheric pressure. By evaluating the *DS* value, it is possible to distinguish between normally-consolidated (NC) soils (OCR = 1) and overconsolidated (OC) soils (OCR >1), and thus estimate σ'_p accordingly:

$$\frac{\sigma'_p}{p_a} = 1.62 \bullet \left(\frac{\sigma'_{v0}}{p_a}\right)^{0.89} \bullet w_L^{0.12} \bullet w_n^{-0.14} \text{ when } DS \leq 1.123 \text{ (very likely NC soils)} \quad \text{(A2a)}$$

$$\frac{\sigma'_p}{p_a} = 7.94 \bullet \left(\frac{\sigma'_{v0}}{p_a}\right)^{0.71} \bullet w_L^{0.53} \bullet w_n^{-0.71} \text{ when } DS > 1.123 \text{ (very likely OC soils)} \quad \text{(A2b)}$$

Appendix B

This Appendix presents weights and biases to apply the developed ML models with simplest topologies indicated in Table 6 for the predictions of G, G/G_0 and D values, knowing the four inputs γ, p'_0, PI and OCR (this order must be respect when applying weights $w_{j1,i}$). Dealing with single-hidden layer networks, the structure illustrated in Fig. 10a can be followed.

Table B1
Weights and biases to derive the output of the jth hidden neuron z_{j1} through Eq. (5) for G predictions (4-13-1 network).

No. Of hidden neuron j	$w_{j1,1}$	$w_{j1,2}$	$w_{j1,3}$	$w_{j1,4}$	$b_{j,1}$
1	0.7155	−5.6207	4.5011	2.9970	2.0049
2	−1.4105	−0.7870	−11.4228	0.8738	1.7639
3	9.4164	−0.6333	0.1515	0.1279	1.6503
4	8.2814	5.8030	1.8012	1.4802	−0.6478
5	0.2728	3.6162	−2.9672	−4.8954	1.7126
6	−0.7424	−1.6355	−4.3920	−0.0451	0.8481
7	0.5920	−1.8180	7.2542	0.4286	−2.4847
8	1.0919	−2.7935	11.7766	1.7107	−4.6211
9	0.1853	−1.0087	−1.3519	−1.7032	0.5202
10	−2.4207	6.5801	−4.9625	−0.2197	−1.5152
11	−0.0385	−3.5137	1.0865	0.3442	−0.1294
12	10.6519	7.5791	2.3452	1.9322	−1.7770
13	1.7179	−7.0950	5.0750	2.4373	2.1834

Table B2
Weights and bias to derive the network output for G predictions through Eq. (6) (4-13-1 network).

No. Of hidden neuron j	$W_{1,j}$	B
1	4.9913	2.3295
2	4.0029	
3	−2.1336	
4	−9.1747	
5	3.0187	
6	−7.8521	
7	−5.5272	
8	2.6063	
9	−3.8870	
10	−1.8688	
11	4.0534	
12	3.1849	
13	−4.4529	

Table B3
Weights and biases to derive the output of the jth hidden neuron z_{j1} through Eq. (5) for G/G_0 predictions (4-9-1 network).

No. Of hidden neuron j	$w_{j1,1}$	$w_{j1,2}$	$w_{j1,3}$	$w_{j1,4}$	$b_{j,1}$
1	−11.3377	−1.5390	−0.4478	0.0535	0.2972
2	8.4138	2.8184	2.6166	0.0859	−1.1581
3	9.8513	5.1928	3.6974	0.3816	−2.3160
4	−1.3542	−0.6834	−4.6159	1.4119	2.8526
5	10.7268	1.2915	−0.1362	2.8246	0.4433
6	9.9257	−0.1855	0.4179	−0.5304	0.6821
7	−1.0417	−0.6547	−6.3197	1.4445	3.5599
8	5.6054	1.0322	2.3452	−0.0313	0.3046
9	−13.1526	0.2226	−0.6383	0.4231	0.0849

Table B4
Weights and bias to derive the network output for G/G_0 predictions through Eq. (6) (4-9-1 network).

No. Of hidden neuron j	$W_{1,j}$	B
1	−3.1293	4.8725
2	−5.4182	
3	2.0182	
4	0.7312	
5	−4.6564	
6	−8.8816	
7	−0.7003	
8	6.5557	
9	−2.4811	

Table B5
Weights and biases to derive the output of the jth hidden neuron z_{j1} through Eq. (5) for D predictions (4-15-1 network).

No. Of hidden neuron j	$w_{j1,1}$	$w_{j1,2}$	$w_{j1,3}$	$w_{j1,4}$	$b_{j,1}$
1	−1.8950	3.4636	−5.5070	1.5086	0.8644
2	0.2256	0.3624	0.1682	0.0396	0.2566
3	−2.7468	−4.9962	−3.6977	1.9412	4.3838
4	2.9348	1.1294	0.5029	−2.9028	−0.1698
5	1.0933	−5.3587	0.7850	0.2699	2.2454
6	0.2594	0.7313	0.2556	0.0153	0.3117
7	0.2504	1.0631	0.3061	−0.0020	0.3875
8	−2.4110	0.9764	0.9764	1.4948	−0.5600
9	−9.0494	2.8293	−3.2191	−0.2688	−1.4399
10	0.2535	1.0285	0.3006	−0.0012	0.3804
11	−1.6938	−8.3731	−2.6557	−1.1247	4.9048
12	0.8719	−6.8338	−4.0136	0.9080	7.2284
13	−0.1905	1.8503	−7.0586	−0.9283	0.5006
14	6.8044	−3.5108	7.4100	3.2517	0.8717
15	6.5285	1.2453	−2.0881	−2.7233	0.3904

Table B6
Weights and bias to derive the network output for D predictions through Eq. (6) (4-15-1 network).

No. Of hidden neuron j	$W_{1,j}$	B
1	4.1618	1.159453
2	0.8674	
3	3.5720	
4	4.3587	
5	5.2661	
6	1.0680	
7	1.2981	
8	−2.2378	
9	−5.7031	
10	1.2732	
11	−3.5211	
12	−2.7646	
13	−4.1388	
14	−6.4195	
15	−2.1795	

Appendix C

This Appendix reviews analytical models from the literature for evaluating the normalized shear modulus G/G_0 and the damping ratio D. For G/G_0, we consider the hyperbolic model initially introduced by Hardin and Drnevich [38] and later modified by Stokoe et al. [71]:

$$\frac{G}{G_0}=\frac{1}{1+\left(\frac{\gamma}{\gamma_{ref}}\right)^{a}} \tag{C1}$$

here, a is a curvature coefficient, and γ_{ref} is the reference strain at which $G/G_0 = 0.5$. Both a and γ_{ref} depend on the confining pressure p'_0, and for fine-grained soils on the Plasticity Index PI and the Over Consolidation Ratio (OCR). Darendeli [40] provided an expression for γ_{ref}. Following recommendations from the literature [46], we have ignored the OCR dependency and calculated γ_{ref} as:

$$\gamma_{ref}(\%)=(\varphi_6+\varphi_7 \bullet PI) \bullet {p'_0}^{\varphi_8} \tag{C2}$$

where φ_6, φ_7 and φ_8 are the modelling parameters. Note that PI is expressed as a percentage and p'_0 in atm. For the D-γ curves, a common approach, starting with Hardin and Drnevich [38] is to relate them to the G/G_0-γ curves as:

$$D=\mathrm{f}(G/G_0)+D_{min} \tag{C3}$$

The following expression for $D_{\min}$ is considered [29,72]:

$$D_{min}=D_{min,1} \bullet (p'_0/p_a)^{-k/2} \tag{C4a}$$

$$D_{min,1}=a_1 \bullet PI+b_1 \tag{C4b}$$

Zhang et al. [29] derived a_1 and b_1 as fitting parameters, equal to 0.008 and 0.82, respectively. They also provided three expressions for k based on PI and geological age (i.e., residual/saprolite soil, tertiary and okler soil, quaternary soil). We selected the expression for residual soils, which provides the best coefficient of correlation R^2 for our database:

$$k=0.42 \bullet e^{-0.0456 \bullet PI} \tag{C5}$$

For the function f (G/G_0) of Eq. (C3), we tested the one presented by Darendeli [40], based on the Masing criteria [73], and another simpler one derived by Zhang et al. [29].

$$\mathrm{f}\left(\frac{G}{G_0}\right)_{\mathrm{Zhang}}=10.6 \bullet \left(\frac{G}{G_0}\right)^2-31.6 \bullet \frac{G}{G_0}+21 \tag{C6}$$

Darendeli's approach can be summarised as:

$$\mathrm{f}\left(\frac{G}{G_0}\right)_{\mathrm{Dar}}=\mathrm{F}\left(\frac{G}{G_0}\right) \bullet D_{Masing} \tag{C7}$$

The function F (G/G_0) is defined as:

$$\mathrm{F}\left(\frac{G}{G_0}\right)=b \bullet \left(\frac{G}{G_0}\right)^{0.1} \tag{C8}$$

where b is a factor that slightly varies with the number of cycles [40,65]. Since we did not investigate this aspect, we assumed it to be constant. The evaluation of D_{Masing} involves the following steps:

$$D_{Masing}=c_1 \bullet \underline{D_{Masing}}+c_2 \bullet \underline{D_{Masing}}^2+c_3 \bullet \underline{D_{Masing}}^3 \tag{C9a}$$

$$\underline{D_{Masing}}=\frac{100}{\pi}\left[4 \bullet \frac{\gamma-\gamma_{ref} \bullet \log\left(\frac{\gamma+\gamma_{ref}}{\gamma_{ref}}\right)}{\frac{\gamma^2}{\gamma+\gamma_{ref}}}-2\right] \tag{C9b}$$

$$c_1=-1.1143 \bullet a^2+1.8618 \bullet a+0.2523 \tag{C9c}$$

$$c_2=0.0805 \bullet a^2-0.0710 \bullet a-0.0095 \tag{C9d}$$

$$c_3=-0.0005 \bullet a^2+0.0002 \bullet a-0.0003 \tag{C9e}$$

We have used the parameter values a (for Eqs. C1 and C9), b (Eq. (C8)), φ_6, φ_7 and φ_8 (to evaluate γ_{ref} through Eq. C2) listed in Table C1. These values were derived by Ciancimino et al. [46] from the dynamic characterisation of 79 samples. This choice was made due to similarities with our tests in terms of i) the soil type investigated (fine-grained soils); ii) the country of origin (Italy, although Ciancimino et al. focused on central Italy while our study is on southern Italy); iii) the laboratory tests performed (RC, TXC and CTS); iv) the plasticity index (PI ranging from 0 to 42 % in Ciancimino et al. from 10.08 to 46 % in our study) and the test confining pressure (p'_0 varying from 30 to 440 kPa in Ciancimino et al. from 60 to 550 kPa in our study).

Table C1
Modelling parameter calibrated by Ciancimino et al. [46].

Parameter	Value
a	0.9640
b	0.5062
φ_6	0.0331
φ_7	0.0014
φ_8	0.1254

Fig. C1 shows the measured G/G_0 against the predicted values, demonstrating a good correlation. Fig. C2 illustrates the application of both Darendeli [40] and Zhang et al. [29] models. In this case, an acceptable accuracy (greater than 0.7) is observed, with Zhang et al. providing the best results. Therefore, the model proposed by Zhang et al. is adopted within this manuscript.

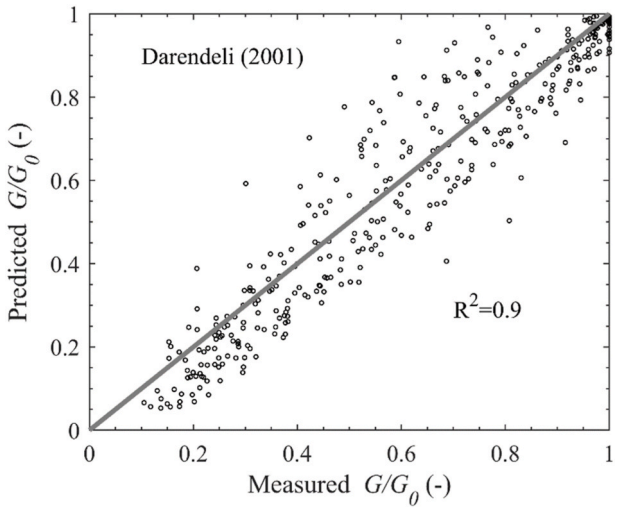

Fig. C1. G/G_0 experimental data vs predictions derived through Darendeli [40].

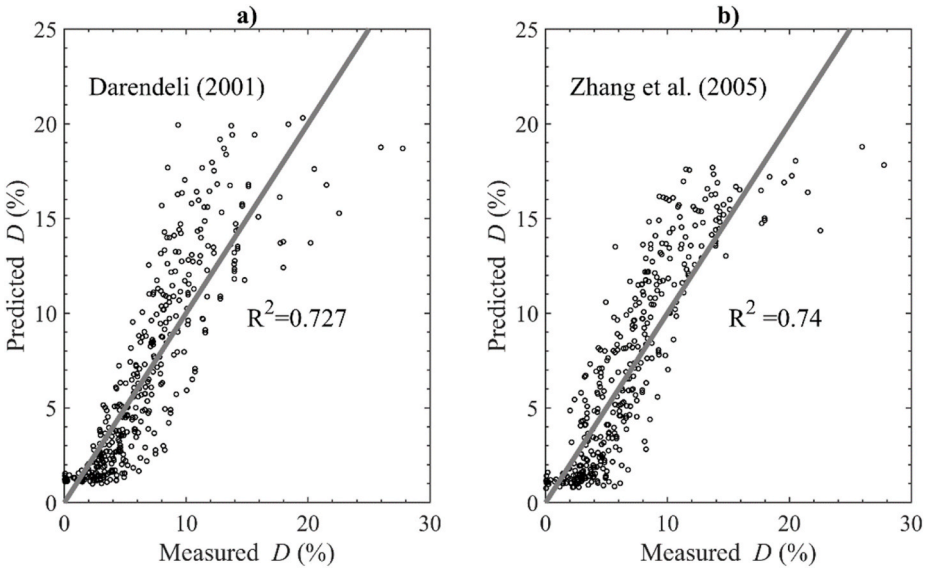

Fig. C2. D experimental data vs predictions derived through a) Darendeli [40] and b) Zhang et al. [29].

Data availability

Data will be made available on request.

References

[1] CEN, EN 1998-1. Eurocode 8: design of structures for earthquake resistance, Part 1: general rules, seismic actions and rules for buildings. Brussels: European Committee for Standardization; 2005.
[2] CS.LL.PP. Decreto Ministeriale del 17/1/2018. Aggiornamento delle "Norme tecniche per le costruzioni G.U. della Repubblica Italiana n.42. 2018 (in Italian).

[3] Pitilakis K, Riga E, Anastasiadis A. New code site classification, amplification factors and normalized response spectra based on a worldwide ground-motion database. Bull Earthq Eng 2013;11:925–66. https://doi.org/10.1007/s10518-013-9429-4.

[4] Chen F, Kang W, Yang Z, Xu L. Seismic pseudo-static active earth pressure of narrow c-φ soils on gravity walls under translational mode. Soil Dynam Earthq Eng 2022;161:107437. https://doi.org/10.1016/j.soildyn.2022.107437.

[5] Sharma S, Prashant A. Seismic coefficients for pseudo-static analysis of wrap-faced GRS walls with nonlinear soil fills. Soil Dynam Earthq Eng 2023;171:107960. https://doi.org/10.1016/j.soildyn.2023.107960.

[6] Castelli F, Lentini V, Maugeri M. One-dimensional seismic analysis of a solid-waste landfill. AIP Conf Proc 2008;1020(PART 1):509–16. https://doi.org/10.1063/1.2963877.

[7] Castelli F, Cavallaro A, Ferraro A, Grasso S, Lentini V. A seismic geotechnical hazard study in the ancient city of noto (Italy). Process Eng 2016;158:535–40. https://doi.org/10.1016/j.proeng.2016.08.485.

[8] Firat S, Isik NS, Arman H, Demir M, Vural I. Investigation of the soil amplification factor in the Adapazari region. Bull Eng Geol Environ 2016;75:141–52. https://doi.org/10.1007/s10064-015-0731-z.

[9] Tsai C, Li P. Quantifying near-fault motion effects on soil liquefaction through effective stress site response analysis. Soil Dynam Earthq Eng 2024;183:108779. https://doi.org/10.1016/j.soildyn.2024.108779.

[10] Che W, Wang W, Chen Z, Ye S. Assessing the effect of input motion duration on seismic site responses of layered soil deposits using spectrally equivalent records. Soil Dynam Earthq Eng 2024;177:108434. https://doi.org/10.1016/j.soildyn.2023.108434.

[11] Abate G, Gatto M, Massimino MR, Pitilakis D, Papadrakakis M, Fragiadakis M. Large scale soil-foundation-structure model in Greece: dynamic tests vs FEM simulation. In: Proceedings of the 6th international conference on computational methods in structural dynamics and earthquake engineering (COMPDYN). Greece: Rhodes Island; 2017.

[12] Cui Z, Zhang L, Zhan Z. Seismic response analysis of shallowly buried subway station in inhomogeneous clay site. Soil Dynam Earthq Eng 2023;171:107986. https://doi.org/10.1016/j.soildyn.2023.107986.

[13] Koronides M, Kontoe S, Zdravković L, Vratsikidis A, Pitilakis D. Numerical simulation of SSI free and forced vibration experiments on real scale structures of different stiffness. Soil Dynam Earthq Eng 2023;175:108232. https://doi.org/10.1016/j.soildyn.2023.108232.

[14] Wang X, Zhao M, Guan J, Yang J, Du X, Zhao X. Site effect on seismic response of buried nuclear power plant structure. Soil Dynam Earthq Eng 2024;183:108759. https://doi.org/10.1016/j.soildyn.2024.108759.

[15] Kanellopoulos C, Rangelow P, Jeremic B, Anastasopoulos I, Stojadinovic B. Dynamic structure-soil-structure interaction for nuclear power plants. Soil Dynam Earthq Eng 2024;181:108631. https://doi.org/10.1016/j.soildyn.2024.108631.

[16] Bahrampouri M, Rodriguez-Marek A, Bommer JJ. Mapping the uncertainty in modulus reduction and damping curves onto the uncertainty of site amplification functions. Soil Dynam Earthq Eng 2019;126:105091. https://doi.org/10.1016/j.soildyn.2018.02.022.

[17] Hu H, Huang Y. PDEM-based stochastic seismic response analysis of sites with spatially variable soil properties. Soil Dynam Earthq Eng 2019;125:105736. https://doi.org/10.1016/j.soildyn.2019.105736.

[18] Shinoda M, Yoshida I, Watanabe K, Nakajima S, Nakamura S, Miyata Y. Seismic probabilistic risk estimation of Japanese railway embankments and risk-based design strength of soil and reinforcement. Soil Dynam Earthq Eng 2022;163:107507. https://doi.org/10.1016/j.soildyn.2022.107507.

[19] Rix GJ, Lai CG, Spang Jr AW. In situ measurement of damping ratio using surface waves. J Geotech Geoenviron 2000;126(5):472–80. https://doi.org/10.1061/(ASCE)1090-0241(2000)126:5(472.

[20] Lai CG, Özcebe AG. Non-conventional lab and field methods for measuring frequency-dependent low-strain parameters of soil dynamic behavior. Soil Dynam Earthq Eng 2016;91:72–86. https://doi.org/10.1016/j.soildyn.2016.09.007.

[21] Kokusho T, Yoshida Y, Esashi Y. Dynamic properties of soft clay for wide strain range. Soils Found 1982;22(4):1–18. https://doi.org/10.3208/sandf1972.22.4_1.

[22] Li D, Liu J, Zou D, Ning F, Zhou C, Jiang Q. Cyclic cumulative strain of coarse-grained soil under large cyclic stress amplitude. Soil Dynam Earthq Eng 2024;183:108748. https://doi.org/10.1016/j.soildyn.2024.108748.

[23] Tsai C-C, Kishida T, Kuo C-H. Unified correlation between SPT–N and shear wave velocity for a wide range of soil types considering strain-dependent behavior. Soil Dynam Earthq Eng 2019;126:105783. https://doi.org/10.1016/j.soildyn.2019.105783.

[24] Menq FY. Dynamic properties of sandy and gravelly soils. Austin, USA: Austin, TX: Department of Civil Engineering, University of Texas; 2003. Ph.D. Thesis.

[25] Senetakis K, Anastasiadis A, Pitilakis K. The small-strain shear modulus and damping ratio of quartz and volcanic sands. Geotech 2012;35(6):1–17. https://doi.org/10.1520/GTJ20120073.

[26] Senetakis K, Anastasiadis A, Pitilakis K. Normalized shear modulus reduction and damping ratio curves of quartz sand and rhyolitic crushed rock. Soils Found 2013;53(6):879–93. https://doi.org/10.1016/j.sandf.2013.10.007.

[27] Dobry R, Vucetic M. Dynamic properties and seismic response of soft clay deposits. In: Proceedings of the international symposium on geotechnical engineering of soft soils, coyoacán, Mexico; 1987.

[28] Vucetic M, Dobry R. Effect of soil plasticity on cyclic response. J Geotech Eng 1991;117(89):89–107. https://doi.org/10.1061/(ASCE)0733-9410(1991)117:1.

[29] Zhang J, Andrus RD, Juang CH. Normalized shear modulus and material damping ratio relationships. J Geotech Geoenviron Eng 2005;131:453–64. https://doi.org/10.1061/(ASCE)1090-0241(2005)131:4(453).

[30] Okur DV, Ansal A. Stiffness degradation of natural fine grained soils during cyclic loading. Soil Dynam Earthq Eng 2007;27(9):843–54. https://doi.org/10.1016/j.soildyn.2007.01.005.

[31] Wang Y, Li S, Duan G, Yin J, Wang Y. Study on dynamic properties of ultrasoft clay based on large amplitude oscillatory shear tests. Soil Dynam Earthq Eng 2023;172:107989. https://doi.org/10.1016/j.soildyn.2023.107989.

[32] Ishibashi I, Zhang X. Unified dynamic shear moduli and damping ratios of sand and clay. Soils Found 1993;33(1):182–91. https://doi.org/10.3208/sandf1972.33.182.

[33] Lanzo G, Vucetic M, Doroudian M. Reduction of shear modulus at small strains in simple shear. J Geotech Geoenviron 1997;123(11). https://doi.org/10.1061/(ASCE)1090-0241(1997)123:11(1035).

[34] Castelli F, Cavallaro A, Grasso S, Lentini V. Undrained cyclic laboratory behavior of sandy soils. Geosciences 2019;9(12):512. https://doi.org/10.3390/geosciences9120512.

[35] Zhou Z, Li G, Shen M, Wang Q. Dynamic responses of frozen subgrade soil exposed to freeze-thaw cycles. Soil Dynam Earthq Eng 2022;152:107010. https://doi.org/10.1016/j.soildyn.2021.107010.

[36] Huang Y, Wang Y, Xu Z, Wang P. Prediction and variable importance analysis for small-strain stiffness of soil based on ensemble learning with Bayesian optimization. Comput Geotech 2023;162:105688. https://doi.org/10.1016/j.compgeo.2023.105688.

[37] Vardanega PJ, Bolton MD. Stiffness of clays and silts: normalizing shear modulus and shear strain. J Geotech Geoenviron Eng 2013;139(9):1575–89. https://doi.org/10.1061/(ASCE)GT.1943-5606.0000887.

[38] Hardin BO, Drnevich VP. Shear modulus and damping in soil: measurement and parameter effects. ASCE Soil Mechan Found Division J 1972;98(6):603–24. https://doi.org/10.1061/JSFEAQ.0001756.

[39] Seed HB, Idriss IM. Soil moduli and damping factors for dynamic response analyses. Berkeley: University of California; 1970 [Report EERC 70-10]. Earthquake Engineering Research Center.

[40] Darendeli MB. Development of a new family of normalized modulus reduction and material damping curves. Austin, USA: University of Texas; 2001. Ph.D. Thesis.

[41] Dai S, Feng S, Lei H, Jia R. A nonlinear dynamic constitutive model of cohesive soil-captured cyclic strain softening characteristics. Soil Dynam Earthq Eng 2024;183:108809. https://doi.org/10.1016/j.soildyn.2024.108809.

[42] Kishida T, Boulanger RW, Abrahamson NA, Wehling TM, Driller MW. Regression models for dynamic properties of highly organic soils. J Geotech Geoenviron 2009;135(4):533–43. https://doi.org/10.1061/(ASCE)1090-0241(2009)135:4(533.

[43] Drosos VA, Gerolymos N, Gazetas G. Constitutive model for soil amplification of ground shaking: parameter calibration, comparisons, validation. Soil Dynam Earthq Eng 2012;42:255–74. https://doi.org/10.1016/j.soildyn.2012.06.003.

[44] Dammala PK, Krishna AM, Bhattacharya S, Nikitas G, Rouholamin M. Dynamic soil properties for seismic ground response studies in Northeastern India. Soil Dynam Earthq Eng 2017;100:357–70. https://doi.org/10.1016/j.soildyn.2017.06.003.

[45] Dammala PK, Kumar SS, Krishna AM, Bhattacharya S. Dynamic soil properties and liquefaction potential of northeast Indian soil for non-linear effective stress analysis. Bull Earthq Eng 2019;17:2899–933. https://doi.org/10.1007/s10518-019-00592-6 (2019).

[46] Ciancimino A, Lanzo G, Alleanza GA, Amoroso S, Bardotti R, et al. Dynamic characterization of fine-grained soils in Central Italy by laboratory testing. Bull Earthq Eng 2020;18:5503–31. https://doi.org/10.1007/s10518-019-00611-6.

[47] Yılmaz MT, Zehtab KH. A practical method for utilization of commercial cyclic testing apparatuses for computation of site response in central Adapazari. Soil Dynam Earthq Eng 2014;63:203–16. https://doi.org/10.1016/j.soildyn.2014.04.003.

[48] Baghbani A, Choudhury T, Costa S, Reiner J. Application of artificial intelligence in geotechnical engineering: a state-of-the-art review. Earth Sci Rev 2022;228:103991. https://doi.org/10.1016/j.earscirev.2022.103991.

[49] Phoon KK, Zhang W. Future of machine learning in geotechnics. Georisk 2022;17(1):7–22. https://doi.org/10.1080/17499518.2022.2087884.

[50] Ghodrati A, Aghaei Araei A. Artificial neural networks for modeling shear modulus and damping behavior of gravelly materials. Int J GeoMech 2017;17(2):04016060. https://doi.org/10.1061/(ASCE)GM.1943-5622.000066.

[51] Islam MS, Rokonuzzaman M. Optimized design of foundations: an application of genetic algorithms. Aust J Civ Eng 2018;16(1):46–52. https://doi.org/10.1080/14488353.2018.1445437.

[52] Ghorbani B, Arulrajah A, Narsilio G, Horpibulsuk S, Win Bo M. Dynamic characterization of recycled glass-recycled concrete blends using experimental analysis and artificial neural network modelling. Soil Dynam Earthq Eng 2021;142:106544. https://doi.org/10.1016/j.soildyn.2020.106544.

[53] Baghbani A, Choudhury T, Samui P, Costa S. Prediction of secant shear modulus and damping ratio for an extremely dilative silica sand based on machine learning techniques. Soil Dynam Earthq Eng 2023;165:107708. https://doi.org/10.1016/j.soildyn.2022.107708.

[54] Gatto MPA, Montrasio L. Artificial Neural Network model to predict the dynamic properties of sand-polyurethane composite materials for GSI applications. Soil Dynam Earthq Eng 2023;172:108032. https://doi.org/10.1016/j.soildyn.2023.108032.

[55] Lendo-Siwicka M, Zabłocka K, Soból E, Markiewicz A, Wrzesiński G. Application of an artificial neural network (ANN) model to determine the value of the damping ratio (D) of clay soils. Appl Sci 2023;13(10):6224. https://doi.org/10.3390/app13106224.

[56] Lbibb S, Manzari MT. Stress-strain behavior of Ottawa sand in cyclic direct simple shear and modeling of cyclic strength using Artificial Neural Networks. Soil Dynam Earthq Eng 2023;164:107585. https://doi.org/10.1016/j.soildyn.2022.107585.

[57] Sun Y, Zhou S, Meng S, Wang M, Mu H. Principal component analysis–artificial neural network-based model for predicting the static strength of seasonally frozen soils. Sci Rep 2023;13:16085. https://doi.org/10.1038/s41598-023-43462-7.
[58] Wu Q, Wang Z, Qin Y, Yang W. Intelligent model for dynamic shear modulus and damping ratio of undisturbed marine clay based on back-propagation neural network. J Mar Sci Eng 2023;11(2):249. https://doi.org/10.3390/jmse11020249.
[59] Charles J, Gourvenec S. GγSANDnet: a neural network tool for prediction of shear stiffness (G) shear strain (γ) relationship for sands. SoftwareX 2024;27:101823. https://doi.org/10.1016/j.softx.2024.101823.
[60] Kootahi K, Mayne PW. Index test method for estimating the effective preconsolidation stress in clay deposits. J Geotech Geoenviron 2016;142(10). https://doi.org/10.1061/(ASCE)GT.1943-5606.00015.
[61] Mohamad HM, Asman NA, Mirasa AK, Saad I, Bolong N, et al. A consistency check of concrete compressive strength using Pearson's correlation coefficient. Civ Eng J 2021;7(3). https://doi.org/10.28991/cej-2021-03091672.
[62] Asghari V, Leung YF, Hsu S-C. Deep neural network based framework for complex correlations in engineering metrics. Adv Eng Inf 2020;44:101058. https://doi.org/10.1016/j.aei.2020.101058.
[63] Kennedy J, Eberhart R. Particle swarm optimization. In: Proceedings of ICNN'95 - international conference on neural networks; 1995. https://doi.org/10.1109/ICNN.1995.488968. Perth, Australia.
[64] Zhao Z, Duan W, Cai G. A novel PSO-KELM based soil liquefaction potential evaluation system using CPT and vs measurements. Soil Dynam Earthq Eng 2021;150:106930. https://doi.org/10.1016/j.soildyn.2021.106930.
[65] Liu P, Qu H, Li J, Ma G. An improved time domain spectral matching method using particle swarm optimization. Soil Dynam Earthq Eng 2024;182:108729. https://doi.org/10.1016/j.soildyn.2024.108729.
[66] McInerney M, Dhawan AP. Use of genetic algorithms with backpropagation in training of feedforward neural networks. In: Proceedings of IEEE international conference on neural networks, San Francisco, CA, USA, 1993; 1993. https://doi.org/10.1109/ICNN.1993.298557.
[67] Lekshmy PR, Raghukanth STG. A hybrid genetic algorithm-neural network model for power spectral density compatible ground motion prediction. Soil Dynam Earthq Eng 2021;142:106528. https://doi.org/10.1016/j.soildyn.2020.106528.
[68] Facciorusso J. An archive of data from resonant column and cyclic torsional shear tests performed on Italian clays. Earthq Spectra 2021;37(1):545–62. https://doi.org/10.1177/8755293020936692.
[69] Khanlari GR, Heidari M, Momeni AA, Abdilor Y. Prediction of shear strength parameters of soils using artificial neural networks and multivariate regression methods. Eng Geol 2012;131:11–8. https://doi.org/10.1016/j.enggeo.2011.12.006.
[70] Merayo D, Rodríguez-Prieto A, Camacho AM. Topological optimization of artificial neural networks to estimate mechanical properties in metal forming using machine learning. Metals 2021;11(8):1289. https://doi.org/10.3390/met11081289.
[71] Stokoe K, Darendeli M, Andrus R, Brown L. Dynamic soil properties: laboratory, field and correlation studies. In: Proceedings of the 2nd international conference earthquake geotechnical engineering, lisboa, Portugal; 1999.
[72] Stokoe K, Hwang S, Lee J-K, Andrus RD. Effects of various parameters on the stiffness and damping of soils at small to medium strains. In: Pre-failure deformation of geomaterials. Proceedings of the international symposium; 1995. Sapporo, Japan.
[73] Masing G. Eigenspannumyen und verfeshungung beim messing. In: Proceedings of international congress for applied mechanics; 1926. p. 332–5.